SAFETY IN MINES RESEARCH ADVISORY COMMITTEE

SIMRAC

Final Project Report

Title: NON-LINEAR SEISMOLOGY

Author/s: A D Dzhafarov
Research

Agency: ISS International

Project No: GAP 211

Date: June 1998

Executive summary

The tendency toward denser, more sensitive seismic networks and the deployment of accelerometers invalidates many assumptions currently used in routine seismological processing. In addition, the routine source parameter inversion is usually done in the frequency domain, discarding all time dependent information contained in the seismograms, basically restricting the inversion procedure to first arrival P and S waves, assuming recording in the far-field and ignoring all near- and intermediate-field radiation effects. As will be shown later, omitting near and intermediate field contributions may have serious consequences for the source parameter inversion results.

The current report deals with some of the problems experienced with recordings made in close proximity to seismic sources. New methods of modelling seismic radiation in the vicinity of the seismic source are proposed, based on the isochron approach. These methods make use of ray theory to model waveforms from finite sources, and allow the selective modelling of propagation effects for the different body wave types in arbitrarily complex three dimensional media.

The other result is the development of a number of signal processing techniques to improve the quality of currently used source parameter inversion methods. The use of adaptive multitaper spectral estimation and the newly developed time domain deconvolution technique significantly reduced spectral variance and improve the quality of low frequency asymptote estimates.

The proposed methods mainly revert from the traditional frequency domain approach to more complicated time domain processing, allowing consideration of the seismic source more realistically as a finite object with finite, but variable, rupture velocity, slip and rake.

The main results may be summarised as follows:

- New signal processing techniques for the inversion of spectral level and corner frequency are developed.
- New procedures for modelling/predicting strong ground motion associated with realistic sources at close distances are developed, and their usage for the inversion of finite seismic sources are conceptualised.

Table of contents

List of figures

List of tables

1 Introduction

An increasing world-wide tendency toward using accelerometers and generally denser three-dimensional seismic networks in the close vicinity of seismic events introduces new type of problems which must be solved in order to perform seismic source inversion.

Heterogeneous materials, such as rock, have extremely non-linear elastic behaviour (the coefficient characterising cubic anharmonicity is several orders of magnitude greater than that of homogeneous materials) and clearly pronounced hysteretic behaviour (the stress-strain equation of state has discrete memory). These effects are usually ignored in routine seismological processing and source inversion.

Existing seismic source inversion theory is based mostly on the assumption of Brune's model and source inversion is usually carried out using linear Green's functions from seismograms recorded in the far field. There are well known difficulties in proper quantification of seismic sources recorded in the intermediate or near field, or at distances less than a few times the predominant wavelength. Inversion becomes even more complex and unstable due to the high degree of nonlinearity of the medium, which causes the mix of different frequency components and elastic energy to transfer from the fundamental frequencies to sum and difference frequencies.

Recently introduced theory of wave propagation in non-linear elastic materials (McCall, 1994, 1995, 1996) explains macroscopic elastic properties of the rock mass as resulting from many mesoscopic hysteretic elastic units. This theory makes use of Preisach-Mayergoyz description of hysteretic systems and effective medium theory to find the quasistatic stress-strain equation of state, the quasistatic modulus-stress relationship, and the dynamic modulus-stress relationship. McCall has proposed further improvement by expressing the non-linear wave propagation in terms of linear Green's functions. This approach is computationally attractive,

The development of procedures for quantification of seismic sources at far, intermediate and near field distances, based on non-linear wave propagation, will lead to better understanding of seismic source radiation and wave propagation in the mining environment.

Time domain processing of waveforms recorded in the vicinity of seismic sources provides some details about the fine structure of the source, such as slip, rake distribution, rupture propagation, nucleation points, etc, along the source surface. With the advent of new methods of numerical modelling of wave propagation based on ray theory, which allow selective modelling of different waves types, this type of inversion is becoming feasible. These methods, operating in time domain, afford a close match between observed and synthetic seismograms at a fraction of the computational cost usually required for this type of inversion by standard finite-difference and finite-element numerical modelling procedures. Newly developed techniques allow separate estimation of near, intermediate and far field contributions for any receiver location and for complex sources. The main idea is to replace the integral along the source surface by a sequence of line integrals along so-called isochrons. The use of isochron formalism reveals a direct link between ground acceleration, rupture acceleration and the spatial variation of the slip on the fault. While the ground motion is indirectly related to rupture velocity, it is directly related to isochron velocity. In this case, separate far, intermediate and near field contributions can be computed, using the same contours of integration -- isochrons. Thus, the algorithm for forward modelling of seismic source radiation both in the near and the far field can be divided in two parts. For stations situated close to source, contributions of the far, intermediate and near fields are calculated. Then an initial far field wavefront is constructed, which will be propagated using the recursive cell ray tracing method. This method, given the initial wavefront, can propagate it throughout the whole model space and can take into account multiply reflected, transmitted, converted and optionally diffracted waves to generate synthetic seismograms for the stations situated in the far field. Another advantage of ray theory based inversion is that for far field synthetic seismograms it is necessary to calculate Green's functions only once, while for standard finite-difference/finite-element techniques Green's functions must be recalculated for every iteration.

This obviously necessitates time-domain treatment for source parameter estimation. The closeness of the seismic sources leads to overestimation of seismic moments and uncertainties in estimates of stress drop and radiated energies. The problem becomes even more complicated when taking into account the nonlinearity of seismic wave propagation. The origin of this phenomenon is inelastic, large strain at the source of a propagating displacement. Thus, in order to obtain proper estimates of seismic source parameters a quite different approach to the inversion problem must be used. These problems have been partially addressed by GAP211.

2 Brune's model in the intermediate field. Novel signal processing techniques to analyse wide band high dynamic range waveforms.

In this section the currently used source parameter estimation techniques are analysed and new methods are proposed to improve the quality of routine seismic inversion procedures.

2.1 Signal processing routines to analyse wide band high dynamic range waveforms

Standard source inversion procedure, currently used in routine seismological processing, is based on Brune's model. Inversion in this case is effectively reduced to spectral estimation of the first P and/or S wave pulse with corrections for geometrical spreading and Q followed by the fitting of Brune's model. Two parameters are inverted, namely, corner frequency and the low frequency asymptote of the displacement spectrum. Estimates of other parameters are obtained analytically based on these two parameters. The simplicity of the above procedure can explain the popularity of Brune's model.

This type of processing relies heavily on the results of the spectral estimation of the displacement spectra of seismic waveforms. Special care needs to be exercised when trying to calculate spectra of wide frequency band and high dynamic range waveforms generated by seismic events and recorded at close distances in mines. The usual approach, consisting in the application of a single time window, e.g. Hanning, Parzen, cosine etc. time windows are frequently inadequate. The application of prolate spheroidal (Slepian) windows allows such problems as energy leakage to be overcome and leads to much more statistically stable spectral estimates. The adopted procedure for the multitaper spectral estimation will be discussed later in this section.

When estimating spectra of seismic waveforms, it is very important to apply some smoothing in the frequency domain. This is necessary primarily because it is almost impossible to obtain the record of the first P or S pulse only. Usually, they are recorded along with other overlapping arrivals (reflected, transmitted, diffracted etc.). The application of a smoothing procedure ensures smoothing out the path effects, while allowing the power spectrum of the first pulse to be obtained. It should be pointed out that the phase information is discarded, so it is impossible to recover the shape of the

waveform in the time domain, unless one makes some simplifying assumption about the phase of the signal: e.g. the signal being minimum or maximum phase.

The standard approach is to use single time domain windows. This approach cannot be recommended for the estimation of the spectra of signals recorded at short distances from the seismic source. Such signals have wide frequency band character and high dynamic range, and the application of such time domain spectral windows as Hamming or Hanning, etc. will emphasise the central part of the signal while underestimating the contribution of the extremes of the input signal.

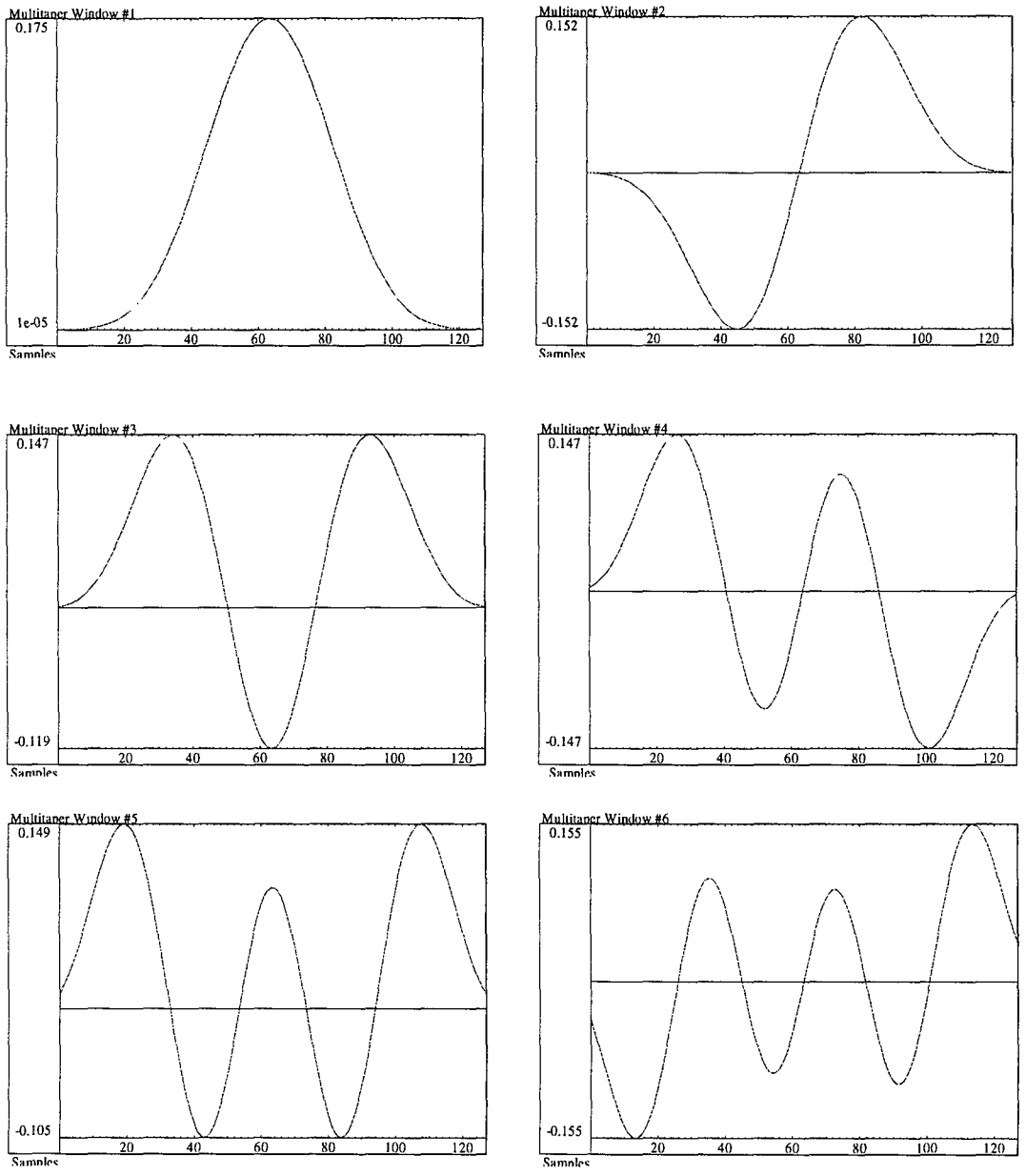

Fig.2-1 The first six discrete prolate spheroidal tapers for N=128 points and time-bandwidth product equal to 4π.

The spectral characteristics of the input signal are not even close to ideal, having relatively wide central lobes and high side lobes, which cause energy leakage in the calculated spectrum from a component with frequency f_o to components in neighbouring frequencies.

One of the possible solutions is to try to use several tapering windows, designed in some way so as to minimise energy leakage. Such windows are obtained as a solution to the following problem:

$$C \bullet \mathbf{v} = \lambda(\mathrm{N}, \mathrm{W}) \bullet \mathbf{v} \tag{2.1}$$

where the matrix C is defined as follows:

$$C_{ik} = \frac{\sin(2\pi W(i-k))}{\pi(i-k)} \tag{2.2}$$

i,k = 0, 1, ..., N-1,
N is number of points in the input time series, and **v** – is the data vector.

Parameter *W,* called the *time-bandwidth product,* controls the degree of smoothness one wishes to achieve. This parameter is very important as the wrong choice of W may lead to overestimation of the low frequency asymptote in the displacement spectra of seismograms. In practice this parameter is expressed as $l/(N \cdot \Delta t)$, where $l = 2,3,4,$ where Δt is the sampling interval of the input time series. Parameter *W* should be set to a higher value if the analysed length of P or S wave includes several predominant periods, and alternatively this value should be reduced if the length of recording expressed in predominant periods is short.

In Fig.2-2 three component seismograms recorded in the near or intermediate field are shown. The spectrum of each component calculated using a Bartlett window are shown in Fig. 2-3 and spectra calculated using the multitaper procedure described above are shown in Fig.2-4. It is obvious that the spectra obtained by the multitaper spectral estimation method give more stable spectral estimates than the single tapered ones, as many local spectral peaks present in the Bartlett windowed spectra are absent in the multitaper estimate.

To further improve the inversion of source parameters a special stacking procedure has been developed. The main idea is to compute individual spectra for all stations in the

event being processed with corrections for geometrical spreading and to try a range of possible Q values. The Q value that gives the best fit for all spectra is chosen as the final Q value and the fit to the Brune's model is done using the final stacked spectrum from all stations.

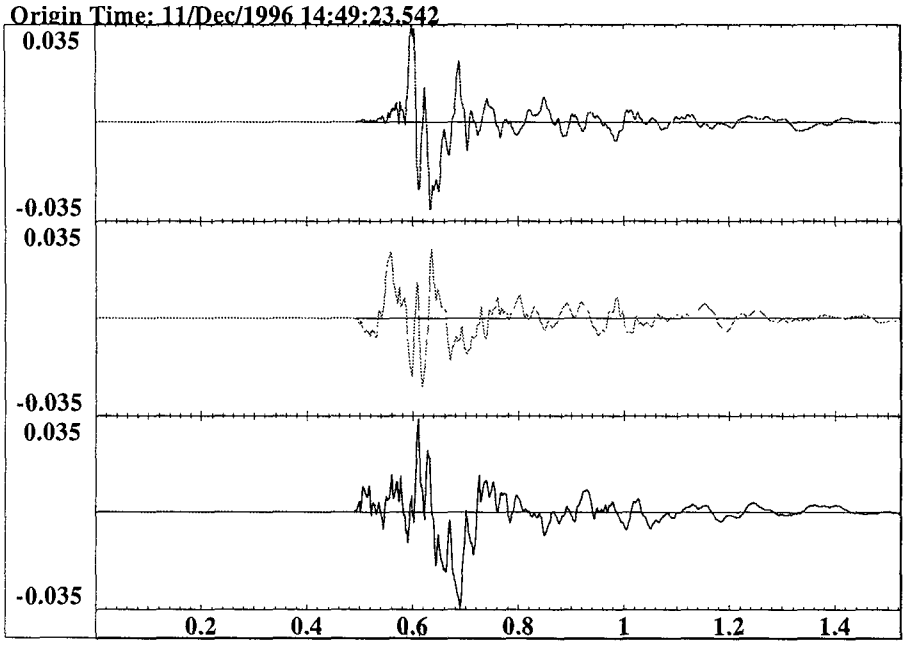

Fig.2-2 Three component velocity seismograms of a seismic event recorded at a hypocentral distance of 449 m. Units on the vertical axis are *m/s*, on the horizontal *s*.

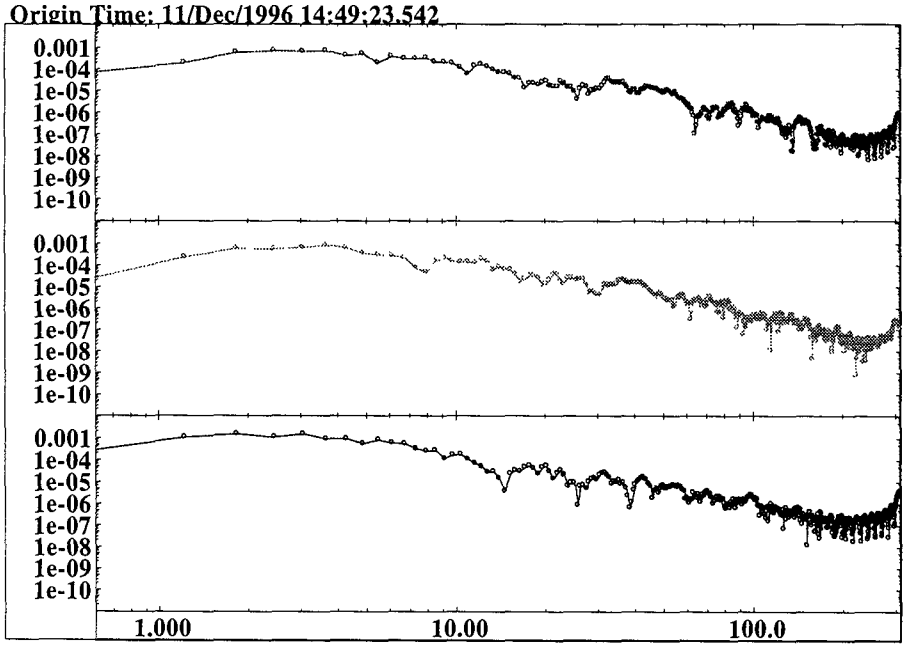

Fig.2- 3 Displacement spectra obtained by a single tapering window application (Bartlett window) to the instrument response deconvolved displacement seismograms. Units on the vertical axis are m*s, on the horizontal Hz.

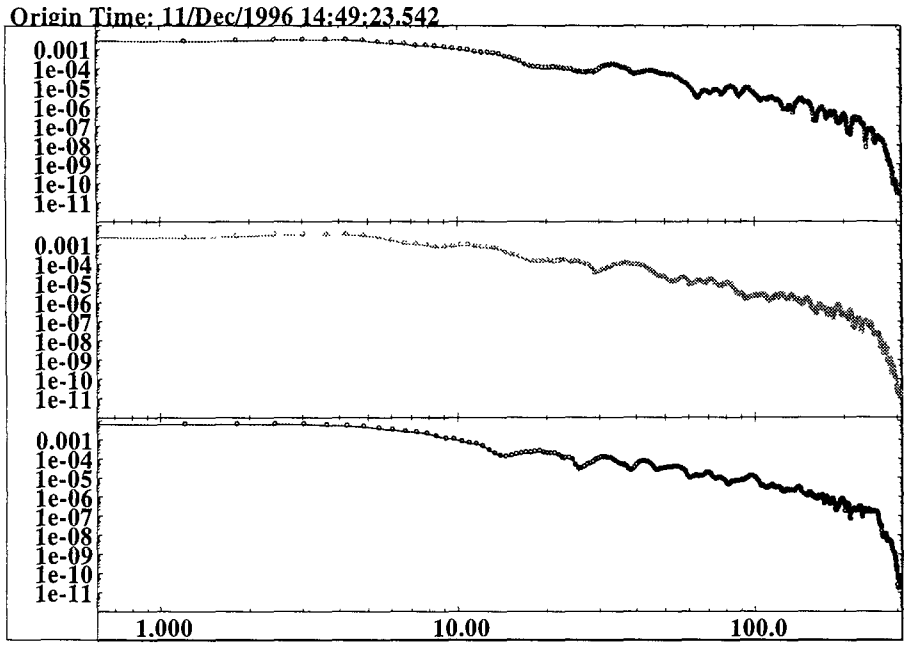

Fig.2-4 Displacement spectra obtained by the application of multitaper spectral analysis (4π bandwidth) to the instrument response deconvolved displacement seismograms. Units on the vertical axis are m*s, on the horizontal Hz. Note the significant reduction of the variance of the spectral estimate in the multitaper estimate.

2.2 Application of Brune's model to spectral analysis of seismic sources recorded in the intermediate field taking into account the effect of source extension.

To take into account the seismic source extension it is necessary to use the Maruyama formula for a dislocation source. This formula describes the displacement vector, caused by a known double couple of forces, which acts at the source of radiation and is valid for a point source only. By integration, it is possible to extend its validity onto a two-dimensional fault. If, in an extended formula, the distance dependent elements with powers one and two are kept, then the result describes the radiation of the far and intermediate fields only, ignoring therefore the contribution of the near field. The displacement spectra are composed of several components with differing distance dependency.

In order to estimate the relative influence of the intermediate field terms on the total radiation, one can run the simulation using a ramp-like source function. Correction for the

influence of the intermediate field on the power displacement spectra can be done the following way:

1. Calculating theoretical power spectra for the given fault at different distances from the fault;
2. Comparing the displacement spectra for two situations: one, where only far field components are present, and the second one, when both intermediate and far field are taking part in forming the total radiated wavefield.

The result of such a simulation, represented as the ratio between the intermediate and far field contributions to the far field contribution only, is shown in Fig. 2-5 for a range of distances.

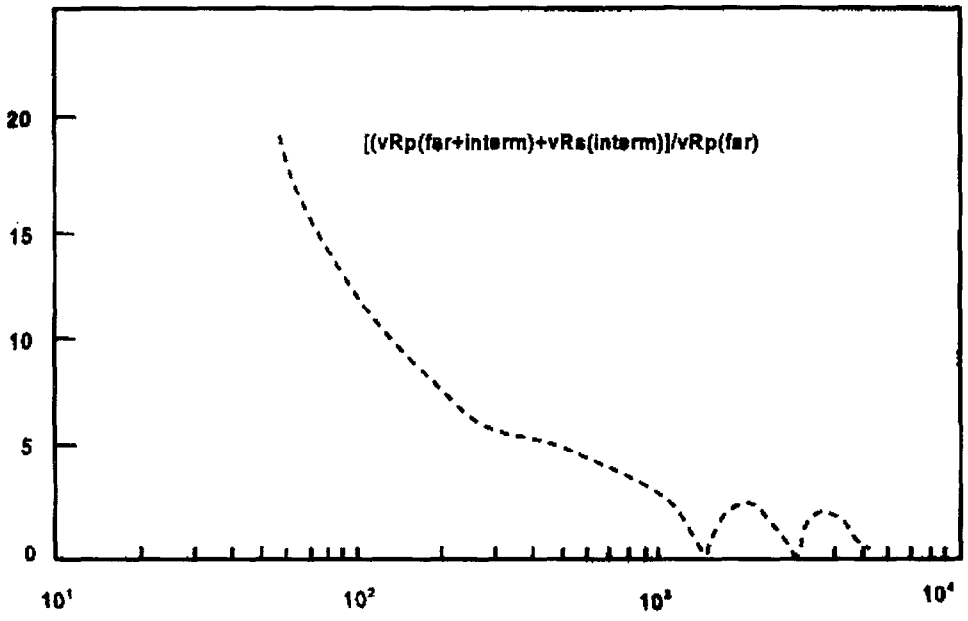

Fig.2-5 The scaling relation showing the influence of the intermediate field radiation on the spectra. The indicated correction factor can be applied to Brune's model parameter inversion of seismograms recorded in the near vicinity of seismic sources. The units on the vertical axis are relative units, on the horizontal axis *m*.

Using the above scaling ratio it is possible to correct the power spectrum for the presence of the intermediate field, and still use Brune's formula to calculate the source parameters. The results obtained are applicable for hypocentral distances shorter than 100 m.

3 Seismic Radiation and the source spectrum – intermediate field.

3.1 Seismic spectra and source time function

The behaviour of seismic waveforms and their spectra reflects the features of the development of the deformation processes in the seismic source. Consideration of waveforms in frequency domain allows the derivation of source dimensions and seismic moment using the values of the corner frequency and the longwave asymptote of the displacement spectrum, using model proposed by Brune. This procedure is widely used for routine seismic source parameter inversion due to its simplicity and the limited number of source parameters to be estimated. However, this frequency domain approach cannot be used for the parameterisation of complex seismic sources. Time domain analysis of observed waveforms allows the construction of a source time function that reflects the heterogeneity of the mechanical properties of the source.

The seismic displacement field, radiated from the seismic source, is described according to the representation theorem as a convolution in the time domain of the moment tensor M and the spatial derivatives of the Green function:

$$\mathbf{u}_n\,(x,t) = \frac{\partial \mathbf{G}_{np}}{\partial \xi_q} \bullet \mathbf{M}_{pq} \qquad (3.1.1)$$

where $\mathbf{u}_n\,(x,t)$ - is the n-th component of displacement at (x,t), due to the varying point force at ξ; $\mathbf{M}_{pq}$ - are components of the moment tensor.

The values G (t) represent the response of the medium to sources acting as elementary dipoles with the time dependence given by a delta-function and are computable from a model of the medium and knowledge of the site and instrument responses. The contribution of each couple forms the moment tensor, which is described in three-dimensional space as a matrix in a Cartesian system of co-ordinates. Due to the involvement of only internal forces in energy radiation from the seismic source, the moment tensor and correspondingly the matrix are symmetrical. Therefore it can always be transformed to the principal axes.

Seismic energy radiated from the seismic source can be represented in the form of elastic waves from a propagating shear dislocation. However, the representation of such a

dislocation as a double couple is just an idealised model, the deviations from which can occur in reality even at low frequencies. One of the basic advantages of the moment tensor description of the seismic source is that it allows the description of non-double couple behaviour of the source and contains information related to the net compression or dilatation within a source and net variation in the orientation of the dislocation.

The representation of the general point seismic source is based on the eigenvalue decomposition of the moment tensor **M**. Let m_1, m_2 and m_3 denote the eigenvalues of the moment tensor **M** and corresponding eigenvectors as $\mathbf{a}_1$, $\mathbf{a}_2$ and $\mathbf{a}_3$. The eigenvalues m1, m_2 and m_3 represent the diagonalised moment tensor, m (it is the same tensor **M**, but in the new orthogonal system of co-ordinates, described by the unit vectors a_1, a_2 and a_3, in which **M** has only diagonal non-zero components). The diagonalised moment tensor m can be decomposed into two major parts: a volumetric part m_v and a deviatoric part, m_D. The volumetric part m_v, is represented by the trace of the tensor M (or m, the trace is not changing by rotation of the system of co-ordinates):

$$\mathbf{m}_v = 1/3\ (m_1 + m_2 + m_3)\ \mathbf{I} = 1/3\ \mathrm{tr}\ (\mathbf{M})\ \mathbf{I} \qquad (3.1.2)$$

where **I** represents a unit matrix.

From the definition of the deviatoric part, m_D, it follows that

$$\mathbf{m}_D = \mathbf{m} - \mathbf{m}_v \qquad (3.1.3)$$

The deviatoric part, m_D, can be further decomposed in several ways. At least two such decompositions have a simple physical meaning: decomposition of m_v into three orthogonal vector dipoles, and into three double couples. The decomposition into three linear vector dipoles is as follows:

$$\mathbf{m}_D = \sum_{i=1}^{3} (m_i - 1/3\ \mathrm{tr}\ (\mathbf{M}))\ \mathbf{a}_i \mathbf{a}_i\ , \qquad (3.1.4)$$

where $\mathbf{a}_i\mathbf{a}_i$ are dyadics. The dyadic $\mathbf{a}_i\mathbf{a}_i$ represents a dipole of unit strength, in which one arm points into the direction of $\mathbf{a}_i$, and the second arm into the direction of $-\mathbf{a}_i$. According to the above representation, the i-th linear dipole is composed of the two equal forces of amplitude $\mathbf{m}_i$ - 1/3 tr (**M**), when the first force points in the direction $\mathbf{a}_i$ and the second one in direction $-\mathbf{a}_i$.

Using the six independent pure double couples, each of which can be represented as follows, can do the second decomposition of the deviatoric part:

$$(m_i - 1/3\,tr\,(\mathbf{M}))\,(\mathbf{a}_i\mathbf{a}_i - \mathbf{a}_j\mathbf{a}_j)\ ,\ i,j = 1,2,3;\ i \neq j\ . \tag{3.1.5}$$

From them it is possible to compose three double couples, using only pairs of the eigenvectors:

$$\mathbf{m}_D = 1/3 \sum_{\substack{i,j=1 \\ i\neq j}}^{3} (m_i - m_j)\,(\mathbf{a}_i\mathbf{a}_i - \mathbf{a}_j\mathbf{a}_j). \tag{3.1.6}$$

In this case, every double couple is composed of two linear vector dipoles, each with the same absolute amplitude $1/3(m_i - m_j)$. If one of these dipoles lies on the direction of the vector $\mathbf{a}_i$, and has the amplitude, say, $1/3(m_i - m_j)$, then the second one has the amplitude $-1/3(m_i - m_j)$ and lies on the direction of the vector a_j. The couple $\mathbf{M}_{ij}$ can be considered as composed one force from the dipole, which lies on the direction of the $\mathbf{a}_i$ vector, and the second force from the dipole, which lies on the direction of $\mathbf{a}_j$ vector.

3.1.1 The case of a synchronous source and the delta source time function

Assumption of a synchronous source means that we assume the same time dependency for every component of the moment tensor. For long period waves, with periods much longer than the rise time of the moment tensor, one may assume that the time derivative of the moment tensor can be treated as the product of the moment tensor and the delta function. If H(t) is a Heaviside step function, and δ(t) is a delta function, then:

$$\mathbf{M}_{pq}(t\ ) = \mathbf{M}_{pq}\,H(t\ );\ d/dt\ \mathbf{M}_{pq}(t\ ) = \mathbf{M}_{pq}\,\delta(t\ ) \tag{3.1.7}$$

The formula for the n-th component of the displacement vector produced by the field of dipoles for the far field is:

$$\begin{aligned} \mathbf{u}_n\,(\mathbf{x},t\ ) = {} & 1/(4\ \pi\rho\alpha^3\ R)\,RP^{far(P)}\ \frac{d}{dt}\ \mathbf{M}_{pq}\ (t\ -\ R/\alpha)\ - \\ & 1/(4\ \pi\rho\beta^3\ R)\,RP^{far(S)}\ \frac{d}{dt}\ \mathbf{M}_{pq}\ (t\ -\ R/\beta) \end{aligned} \tag{3.1.8}$$

or, in a simplified way:

$$\mathbf{u}_n(x,t) = 1/(4\pi\rho\alpha^3 R)\, RP^{far(P)}\, \mathbf{M}_{pq}\,\delta(t - R/\alpha) - 1/(4\pi\rho\beta^3 R)\, RP^{far(S)}\, \mathbf{M}_{pq}\,\delta(t - R/\beta) \quad (3.1.9)$$

where M_{pq} represents the value of the *pq* tensor component at the source, and the displacement component is recorded at the time t-R/α for the P waves, and at the time t - R/β for the S waves, $RP^{far(P)}$ and $RP^{far(S)}$ are radiation patterns.
In this case, the moment tensor elements can be calculated in the time domain or in the frequency domain, on the basis of the equation (3.1.8).

3.1.2 The case of the asynchronous source and arbitrary source time function.

The often-made assumption that all moment tensor components have the same time dependency is a very restrictive one. In the case of seismic events in mines, where volumetric changes of the source region are significant, it is reasonable to take into account differing time dependencies of different moment tensor components. That allows us to reconstruct the source mechanism changes with time throughout the time history of moment tensor components.

Outlined below is the procedure for the time-dependent moment tensor inversion for P waves only (the extension of this procedure to the case of S waves, is rather straightforward). In the remainder of the discussion attention is restricted to the far and intermediate radiation fields, neglecting the near field radiation. To calculate the six moment tensor components, the data from at least six seismic stations are required. We will use only the radial P wave component of displacement. The far field displacement only has a radial component in the far field, but it should be noted that in the case of the intermediate field a transverse component is present as well.

In the far field the radial component of the displacement, for which the moment tensor components from the main diagonal are responsible, can be expressed as follows:

$$U_r(t) = (\gamma_i^2) / (4\pi\rho\alpha^3 R)\, \frac{d}{dt} M_{ii}(t - R/\alpha) \quad (3.1.10)$$

where λ_i are the directional cosines of the seismic ray, α is the P-wave velocity, ρ is the rock density, and R is the distance from the source to the station along the seismic ray. The radial component of the far field created by the off-diagonal moment tensor components, $M_{ij}(.)$, i,j = x,y,z, depends on two directional cosines γ_i and γ_j:

$$U_r(t) = (2\gamma_i\gamma_j)/(4\pi\rho\alpha^3 R)\frac{d}{dt}M_{ij}(t - R/\alpha) \quad (3.1.11)$$

For the intermediate field from the representation theorem yields the following equations:

$$U_r(t) = (4\gamma_i^2 - 1)/(4\pi\rho\alpha^2 R^2)\, M_{ii}(t - R/\alpha) \quad (3.1.12)$$

for the diagonal moment tensor components, M_{ii} (.), and for the off-diagonal moment tensor components, M_{ij} (.):

$$U_r(t) = (8\gamma_i\gamma_j)/(4\pi\rho\alpha^2 R^2)\, M_{ij}(t - R/\alpha) \quad (3.1.13)$$

In order to calculate the moment tensor components one needs to solve a system of differential equations, which follow from the last four expressions.
Below are shown some results of application of the above moment tensor inversion procedure are shown.

Fig.3.1 (a,b) show the results of the moment tensor calculation for the seismic events (a) with M=0.4 and the blast (b), M=0.2

Fig.3.2(a,b) show the radial components of displacement.

Fig.3.3 (a,b) show the decomposition of the estimated moment tensors into deviatoric and isotropic components.

Fig.3.4 (a,b) show stereographic projections of the smallest P (o) and greatest T (x) eigenvectors.

As can be seen the principal axes orientation for these events prove to be stable and provide results which are consistent with the observed P wave first-motion distribution. It should be noted that MT estimation of the principal moment orientation can be obtained using far fewer stations than are required for first motion focal mechanism solutions.

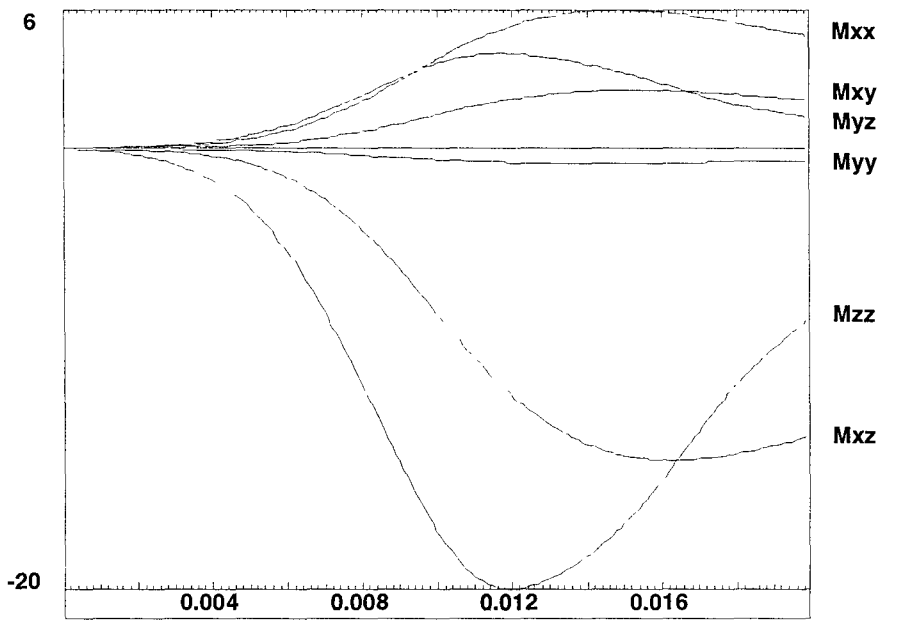

Fig. 3.1 a M = 0.4

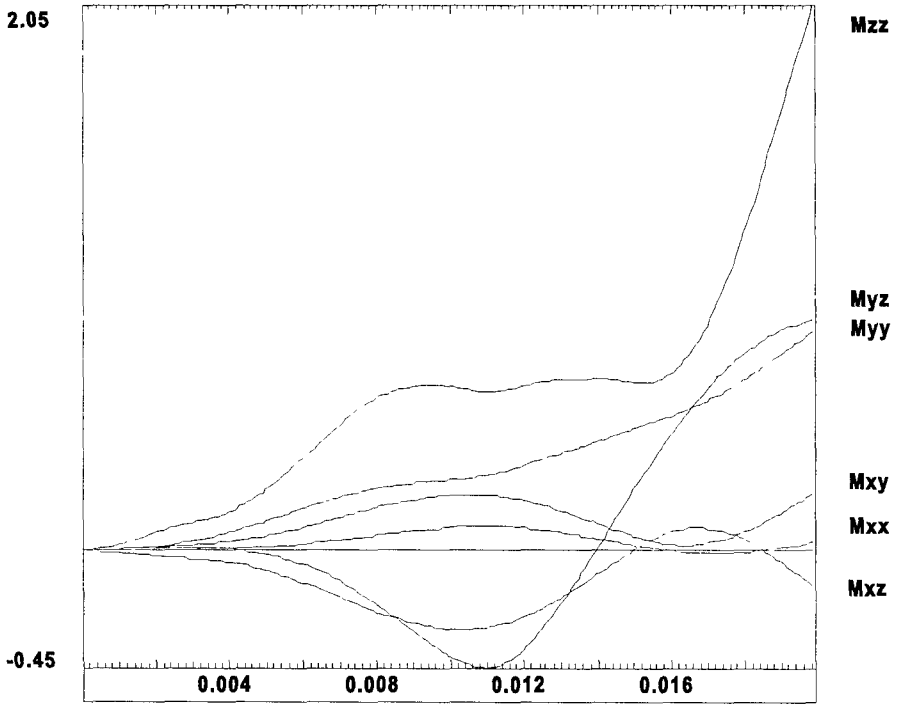

Fig. 3.1.b M = 0.2 (Blast)

Fig.3-1 Time varying moment tensor components calculated for events of various magnitudes. One unit on the vertical axis corresponds to 10^{10} Nm. Note the very short rise time of the moment tensor components

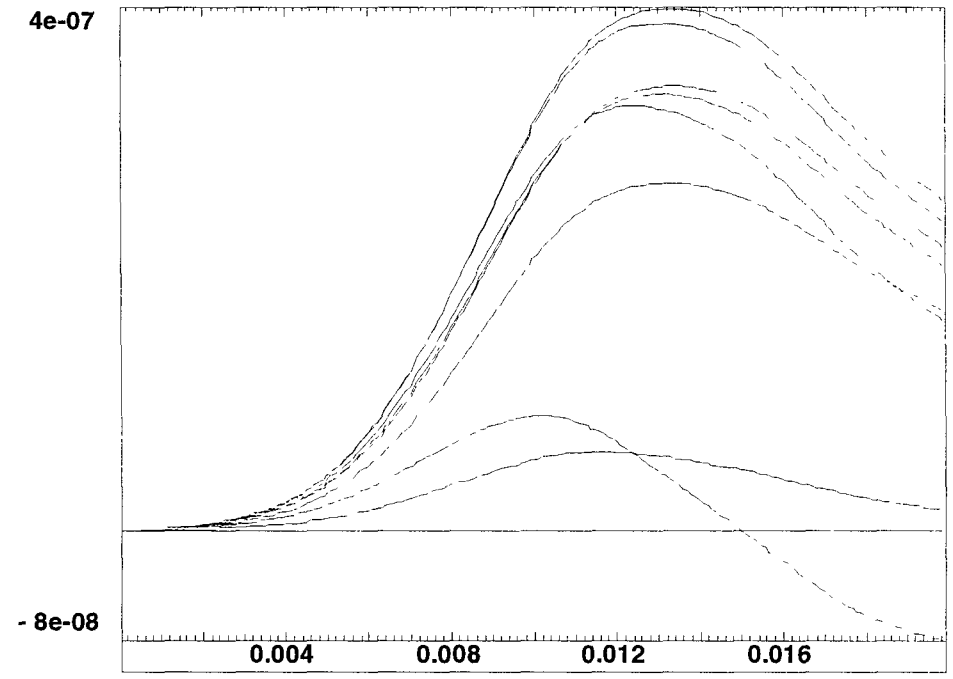

Fig.3-2a M = 0.4

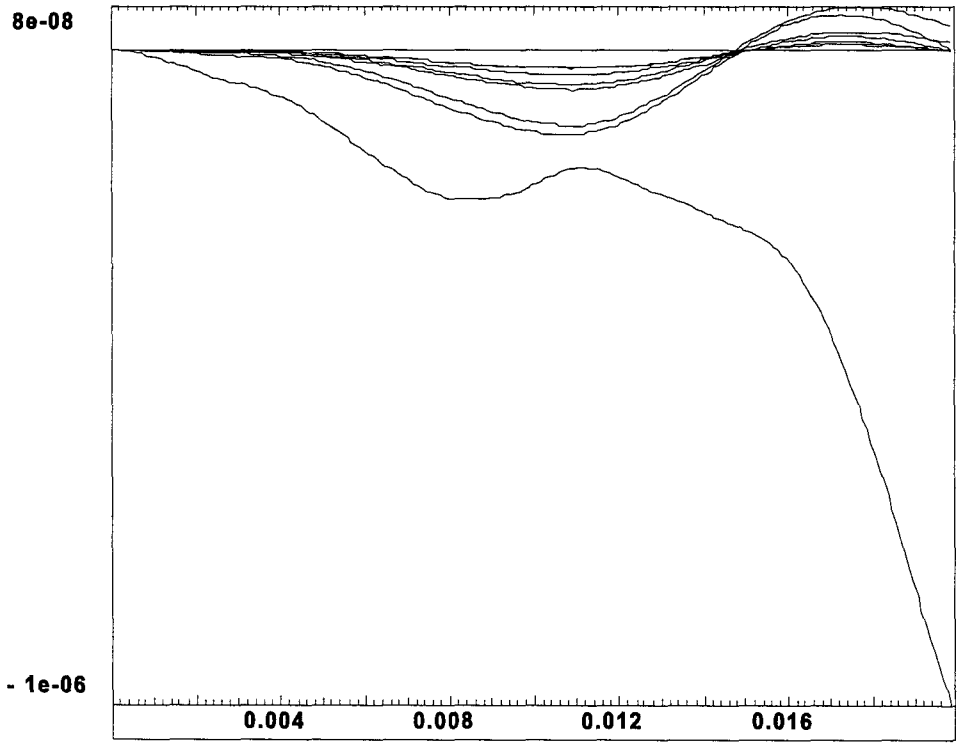

Fig. 3-2b M = 0.2 (Blast)

Fig.3-2 Radial components of displacement due to events of various magnitudes. One unit on the vertical scale corresponds to 10^{10} Nm.

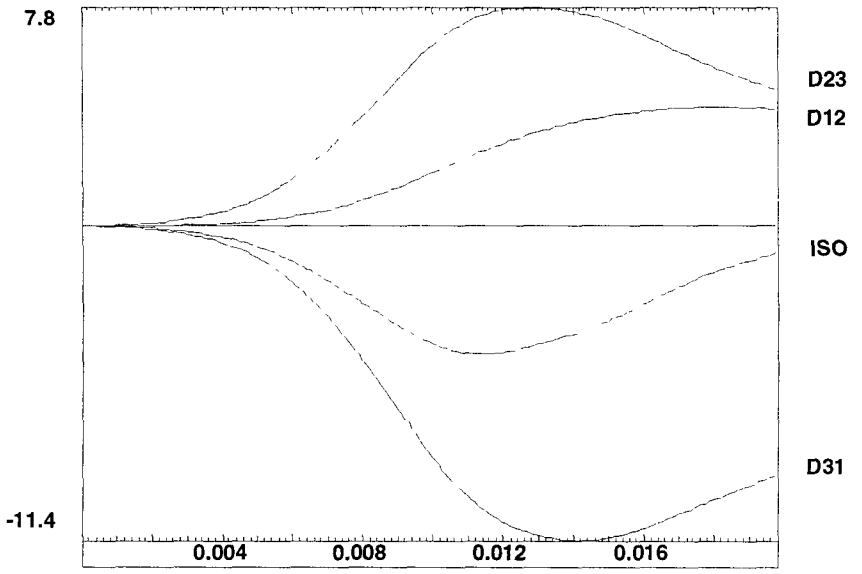

Fig.3-3a M = 0.4

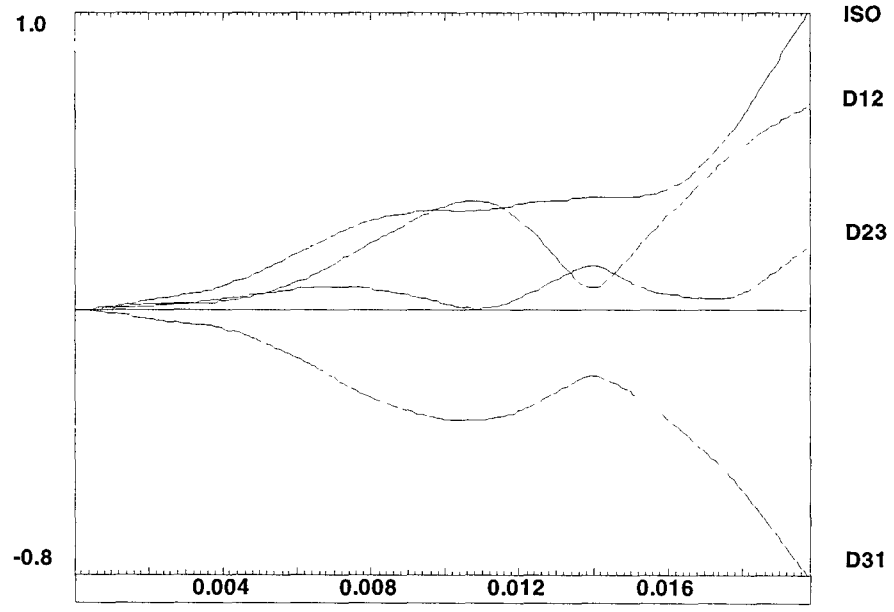

Fig.3-3b M = 0.2 (Blast)

Fig.3-3 Deviatoric (D12, D23, D31) and volumetric (ISO) parts of the moment tensors calculated for events of various magnitudes. One unit on the vertical scale corresponds to 10^{10} Nm.

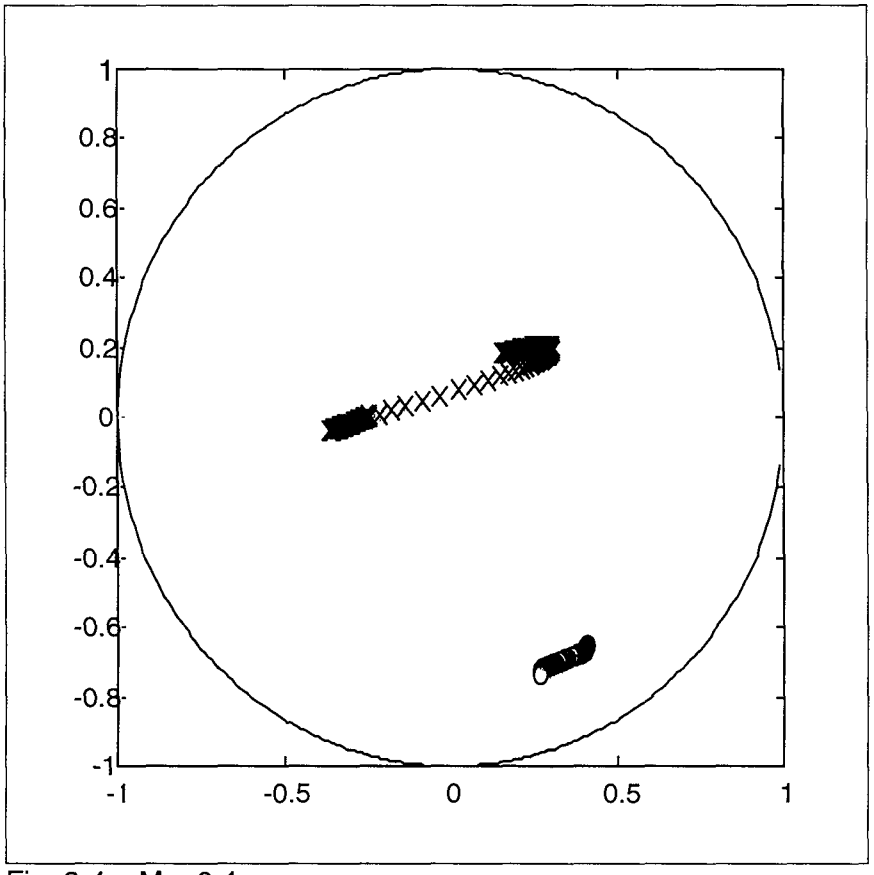

Fig. 3-4 a M = 0.4

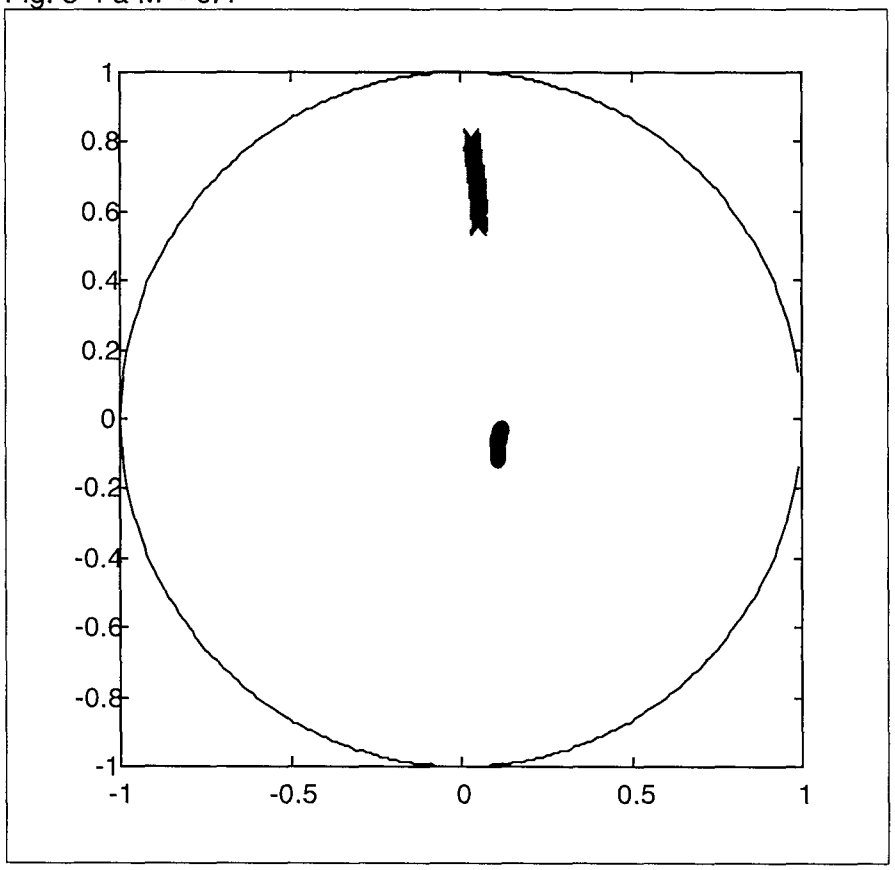

Fig. 3.4b M = 0.2 (Blast)

Fig.3-4 Stereographic projection of the greatest T and smallest P eigenvectors of events of various magnitudes. Variation in the T axis is denoted by X and in the P axis the by 0.

3.2 Non-linear interactions of frequency components of large amplitude elastic waves

As was mentioned earlier, seismic wave propagation in the close vicinity of seismic sources exhibits strongly non-linear behaviour. In this section some results of the study of non-linear wave propagation phenomena are described, namely non-linear wave self - interaction, i. e., two waves from the same source interfere, but not according to a linear superposition principle.

The origin of this phenomenon is inelastic, large strain at the source of a propagating displacement. The result is that the wave propagation can be viewed in two ways:

- A source initiates waves, some of which can propagate freely to the observation point, while some can interfere several times along the way with each other. The sum of all these possibilities is the final observed wave. The important fact is that, for inelastic deformations, the amplitudes of interfering waves do not add together in a simple algebraic fashion, but are actually multiplied. The interference terms also have linear dependence on distance from the source, suggesting that at large distances they will become dominant in the observed spectrum.
- Instead of considering propagating waves from the same source, one can visualise an extended source with secondary sources responsible for higher-order non-linear terms in observed spectra.

The problem here is whether the higher-order terms do indeed appear in our data or whether we do not see many of them because of observational difficulties.

We have used recently developed non-linear wave propagation theory in order to describe non-linear wave propagation effects.

This is based on considering the strain tensor up to second order:

$$\varepsilon_{ij} = \frac{1}{2}\left(\frac{\partial u_i}{\partial x_j} + \frac{\partial u_j}{\partial x_i} + \frac{\partial u_l}{\partial x_i}\frac{\partial u_l}{\partial x_j}\right) \tag{3.2.1}$$

with u_i the displacement or deformation of a generic particle of the medium.

The equation of motion for a wave propagating in a medium is

$$\rho\frac{\partial^2 u_i}{\partial t^2} = \frac{\partial \sigma_{ij}}{\partial x_j} + f_i \tag{3.2.2}$$

where ρ is the density of the medium, σ_{ij} is the internal stress tensor and f_i is an external force that initiates the medium response. The above equation can be written

$$\rho \frac{\partial^2 u_i}{\partial t^2} - \frac{\partial}{\partial x_j}(c_{ijkl}\frac{\partial u_k}{\partial x_l}) = f_i \tag{3.2.3}$$

where one uses

$$\sigma_{ij} = c_{ijkl}\frac{\partial u_k}{\partial x_l} \tag{3.2.4}$$

In the case of an isotropic medium, the elastic modulus tensor can be written

$$c_{ijkl} = \lambda \delta_{ij}\delta_{kl} + \mu(\delta_{ik}\delta_{jl} + \delta_{il}\delta_{jk})$$

and equation (3.2.3) becomes

$$\rho \frac{\partial^2 u_i}{\partial t^2} - (\lambda + \mu)\frac{\partial^2 u_i}{\partial x_i \partial x_i}) - \mu \Sigma_j \frac{\partial^2 u_i}{\partial x_j \partial x_j}$$

$$= f_i + (\lambda + \mu)\Sigma_{k\neq i}\frac{\partial^2 u_k}{\partial x_i \partial x_k}$$

All repeated indices in Equation (3.2.4) above are summed. We would now like to consider the form of u(x,t) at position x and time t when the initiating force f_i had acted at a different position x' at a time t' < t earlier. The displacement u(x,t) will clearly be the initial displacement u(x',t'), modified by the action of the external force, the medium and interactions with other waves along the way. This modification is described by a Green's function. First consider the case where no interactions occur during propagation. We change to a so-called helicity basis, i. e., to one direction of propagation, call it x_L, and two transverse directions x_{Ti}, I=1,2. The equations of motion then become

$$\frac{1}{c_\alpha^2}\frac{\partial^2 u_L}{\partial t^2} - \frac{\partial^2 u_\alpha}{\partial x_L^2} = \frac{f_i}{K_\alpha} \tag{3.2.5}$$

where α = L, T_{Ti} and

$$c_\alpha^2 = \frac{\lambda + 2\mu}{\rho}$$

$$c_{Ti}^2 = \frac{\mu}{\rho}$$

$$K_L = \lambda + 2\mu$$

$$K_{Ti} = \mu$$

In this case, the free Green's function is defined by

$$(\frac{1}{c_\alpha^2}\frac{\partial^2}{\partial t^2} - \frac{\partial^2}{\partial x_L^2})G_\alpha^0(x,x') = \delta^3(\vec{x} - \vec{x}')\delta(t - t')$$

where x ≡ (**x**,t). One finds

$$u_\alpha^0 = \int d^4x' G_\alpha^0(x,x') \frac{f_\alpha(x')}{K_\alpha} \tag{3.2.6}$$

with $d^4x' \equiv dV'dt'$ for a wave initiated at (**x**',t') and travelling freely to (**x**,t). Note that equation (1.2.6) describes the propagation of a wave initiated by f and then travelling freely.

When the second-order terms are taken into account, the equation of motion is

$$\frac{1}{c_L^2}\frac{\partial^2 u_L}{\partial t^2} - \frac{\partial^2 u_L}{\partial x_L^2}$$

$$= \frac{f_L}{K_L} + g_L \frac{\partial}{\partial x_L}\left(\frac{\partial u_L}{\partial x_L}\right)^2 + g_{TL}\frac{\partial}{\partial x_L}\left[\sum_{i=1}^{2}\left(\frac{\partial u_{Ti}}{\partial x_L}\right)^2\right] \tag{3.2.7a}$$

and

$$\frac{1}{c_{Ti}^2}\frac{\partial^2 u_{Ti}}{\partial t^2} - \frac{\partial^2 u_{Ti}}{\partial x_L^2} = \frac{f_{Ti}}{K_{Ti}} + g_T \frac{\partial}{\partial x_L}\left(\frac{\partial u_L}{\partial x_L}\frac{\partial u_{Ti}}{\partial x_L}\right) \tag{3.2.7b}$$

Writing down the Lagrangian density of the system above is instructive, since the Lagrangian is essentially the difference between the kinetic and potential energy of the field u_α:

$$L_L = \frac{1}{2c_L^2}\left(\frac{\partial u_L}{\partial t}\right)^2 - \frac{1}{2}\left(\frac{\partial u_L}{\partial x_L}\right)^2 + \frac{f_L}{K_L}u_L$$

$$- \frac{g_L}{3}\left(\frac{\partial u_L}{\partial x_L}\right)^3 - g_{TL}\left[\sum_{i=1}^{2}\left(\frac{\partial U_{Ti}}{\partial x_L}\right)^2\right]\frac{\partial u_L}{\partial x_L} \tag{3.2.8.a}$$

and

$$L_T = \frac{1}{2c_{Ti}^2}\left(\frac{\partial u_{Ti}}{\partial t}\right)^2 - \frac{1}{2}\frac{\partial u_{Ti}}{\partial x_L}\Big)^2$$

$$+ \frac{f_{Ti}}{K_{Ti}}u_{Ti} - \frac{g_T}{2}\frac{\partial u_L}{\partial x_L}\left(\frac{\partial U_{Ti}}{\partial x_L}\right)^2 \tag{3.2.8b}$$

In, for example, (3.8a), the potential energy is

$$V = +\frac{1}{2}\left(\frac{\partial u_L}{\partial x_L}\right)^2 - \frac{f_L}{K_L}u_L$$

$$+\frac{g_L}{3}\left(\frac{\partial u_L}{\partial x_L}\right)^3 + g_{TL}\left[\sum_{i=1}^{2}\left(\frac{\partial U_{Ti}}{\partial x_L}\right)^2\right]\frac{\partial u_L}{\partial x_L}$$

$$\equiv V_0 + V_C + V^{(3)} + V^{TL}$$

where V_0 is the potential energy of the usual configuration, V_C is the potential energy associated with the initial propagation and creation of the wave, $V^{(3)}$ is the energy associated with a third-order (cubic-anharmonic) interaction between derivative waves and V^{TL} is a cubic interaction between transverse and longitudinal components. Then

$$g_L = \frac{1}{2}\frac{3(\lambda + 2\mu) + 2(l + 2m)}{\lambda + 2\mu}$$

$$g_{TL} = \frac{1}{2}\frac{\lambda + 2\mu + m}{\lambda + 2\mu}$$

$$g_T = \frac{\lambda + 2\mu + m}{\mu}$$

are the strengths of the interactions, λ, μ being first-order elastic constants and l, m second order.

The full Green's function obeys

$$\frac{1}{c_L^2}\frac{\partial^2}{\partial t^2} - \frac{\partial^2}{\partial x_L^2}G_L(x,x')$$

$$= \delta^3(\vec{x} - \vec{x}')\delta(t - t')$$

$$+ g_L\frac{\partial}{\partial x'_L}\left(\frac{\partial G_L(x,x')}{\partial x'_L}\right)^2 + g_{TL}\frac{\partial}{\partial x'_L}\left[\sum_{i=1}^{2}\left(\frac{\partial G_{Ti}(x,x')}{\partial x'_L}\right)^2\right]$$

with solution of the form

$$G = G^0 + G^0 V G^0 + G^0 V G^0 V G^0 + \ldots$$

so that, up to first order,

$$u_L(\vec{x},t) = u^0(\vec{x},t)$$

$$+ g_L \int d^4 x' G_L^0(x,x') \frac{\partial}{\partial x'_L} \left(\frac{\partial u^{0_L}(x')}{\partial x'_L} \right)^2 \qquad (3.2.9)$$

$$+ g_{TL} \int d^4 x' G_L^0(x,x') \frac{\partial}{\partial x'_L} \left[\sum_{i=1}^{2} \left(\frac{\partial u^{0_{Ti}}(x')}{\partial x'_L} \right)^2 \right]$$

An explicit solution for G^0 can be found in the frequency domain, which leads in a tedious fashion to the solution, to first order, for u. With $f_L = -2i\chi(\omega)A_L(\omega)U_L\delta(x_L)F(\omega)$, $f_{T1} = -2i\chi(\omega)A_{T1}(\omega)U_T\delta(x_{T1})F(\omega)$ and $f_{T2} = 0$ where $\chi(\omega)$ is an attenuation factor, $A_L(\omega)$ a wavenumber factor and U_L the amplitude of the initial disturbance,

$$u_L^0 = U_L F(\omega) e^{iA_L(\omega)x_L}$$

$$u_L^1 = g_L U_L^2 x_L E_L + g_{LT} U_T^2 x_L E_{TT}$$

where the important features are the amplitude-squared dependence of the first order non-linear term, as well as its proportionality to propagation distance x_L. A variety of initiating forces $F(\omega)$ can be tried, such as continuous single - frequency sine wave and broadband sources such as

$$F(\omega) = \frac{\Omega}{(i\omega - \Omega)^2}$$

For our purposes, the distance dependence and, since for periodic waves the first-order non-linear terms are second harmonics with frequency twice that of u^0, high frequencies, complicate matters in the observation of non-linear propagation effects.

In Fig.3-5 we have shown the theoretical spatial alteration of displacement spectra for receivers at different distances from the source. The most noticeable property is the increase in high frequency amplitude region for the remote station compared to that, which is situated very close to the source.

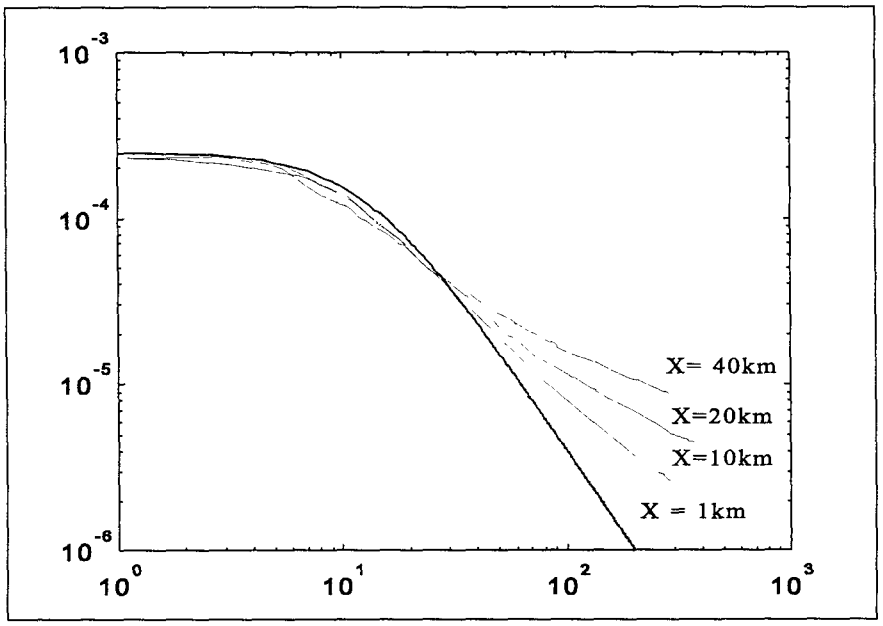

Fig.3-5. Theoretical spatial alteration of displacement spectra from a broadband seismic source in the presence of nonlinearity and attenuation (after McCall, 1994). The pulse propagates to the distances of 1, 10, 20 and 40 km. Units on the vertical axis are in m*s, on the horizontal axis, in Hz.

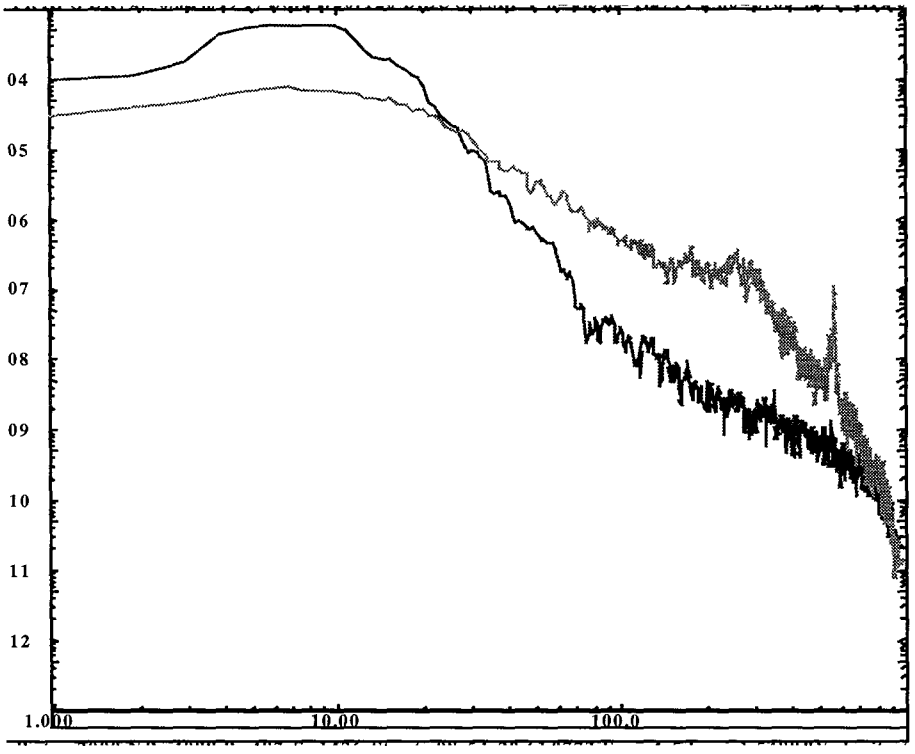

Fig.3-6 Displacement spectra for the S wave for a seismic event which occurred on 06 Jan 1997 at two stations, one situated close to the source (hypocentral distance is 842 m) shown as a solid line, the other distant (distance is 3230m). Seismograms have been deconvolved for the instrument response and integrated to displacement, prior to the application of a multitaper spectral estimation. Non-linear propagation effects are clearly observed in the high-frequency region. Units on the vertical axis are in m*s, units on the horizontal axis in Hz.

When applied to a simple unidirectional source and simplest Green function the above formalism predicts that in broadband signals, each individual spectral component produces a second harmonic and a sum and difference with every other component, expanding the spectrum of the original signal to both the low and high frequency ends. It must be pointed out that the high-frequency contribution is much more distinct. Therefore, the obvious direction of further research is to compare the displacement spectra in the near vicinity of the source and the spectra of signals recorded at more remote stations.

If such a non-linear wave propagation phenomenon exists, then one should be able to observe it as mostly discrepancies between displacement spectra for seismic stations close to the source and at some distance. It should be noted that the above non-linear wave propagation theory predicts not only an increase in high frequency content with the distance from the source, but also changes in the low frequency region as well. However, such phenomena would be very difficult to observe in the low frequency region, due to the type of instrumentation currently deployed in mines - short period geophones and accelerometers.

Let us now consider an example of observed nonlinearity of wave propagation. In Fig.3-6 the spectra of S waves recorded from the same source but at different distances are shown. One can observe the increase in high-frequency content at the distant station compared to the spectrum of S wave recorded close to the source, which cannot be explained using linear wave propagation theory.

The most important conclusion, which follows from a close consideration of (3.2.9), is that the non-linear wave propagation can be expressed in terms of a linear Green's function. Taking into account non-linear contribution to the total observed wavefield, the Green's function technique may be formulated as follows:

- The system is initially disturbed by an external source;
- The Green's function describes the propagation of the displacement field from this disturbance;
- In the interior of this system the nonlinearity acts on the displacement field to produce an internal source.
- The Green's function is used to propagate again the effect of this internal source to the receiver.

Therefore, seismic forward modelling of non-linear wave propagation can be implemented in a simple way, using well-known algorithms of linear wave propagation.

3.3 Seismic Radiation in the intermediate field

The displacement caused by the unit force applied at the source at the time moment τ, can be expressed by the following modification of the Stokes' solution for the Green's function in an infinite homogeneous media:

$$G_{nm}(\mathbf{x},t;\zeta,\tau) = \frac{1}{4\pi\rho}(3\gamma_n\gamma_m - \delta_{nm})\frac{1}{R^3}\int_{R/\alpha}^{R/\beta}\tau'\,\delta(t-\tau-\tau')\,d\tau' +$$

$$\frac{1}{4\pi\rho\alpha^2}\gamma_n\gamma_m\frac{1}{R}\,\delta\left(t-\tau-\frac{R}{\alpha}\right) - \frac{1}{4\pi\rho\beta^2}(\gamma_n\gamma_m - \delta_{nm})\frac{1}{R}\,\delta\left(t-\tau-\frac{R}{\beta}\right)$$

where $G_{nm}(\mathbf{x},t;\zeta,\tau)$ is the Green's function for an infinite, homogeneous media for a displacement caused by a single force $F(\zeta,\tau)$ applied at the point ζ, and at the time τ, and acting in the $\mathbf{x}_m$ direction; α is the P-wave velocity, β is the S-wave velocity, γ_n, γ_m are directional cosines of the vector $\mathbf{x}-\boldsymbol{\zeta}$, ρ is the rock density, R is the distance between receiver and source, and δ Dirac's delta function. In the above equation the first term describes the near field, while the second and third terms describe the far field contribution. In the far field the P-waves have radiation factor $\gamma_n\,\gamma_m$, which specifies the longitudinal displacement of the particles of the medium, and $(\lambda_n\,\lambda_m - \delta_{nm})$ for S waves, which corresponds to the direction perpendicular to the vector $(x-\zeta)$. Substituting the above equation into the representation theorem equation, we obtain the following equation

$$\mathbf{u}_n(x,t) = RP^{near}\frac{1}{4\pi\rho}\frac{1}{R^4}\int_{R/\alpha}^{R/\beta}\tau\,M_{pq}(t-\tau)\,d\tau$$

$$+ RP^{interm(\alpha)}\frac{1}{4\pi\rho\alpha^2}\frac{1}{R^2}M_{pq}\left(t-\frac{R}{\alpha}\right) - RP^{interm(\beta)}\frac{1}{4\pi\rho\beta^2}\frac{1}{R^2}M_{pq}\left(t-\frac{R}{\beta}\right)$$

$$+ RP^{far(P)}\frac{1}{4\pi\rho\alpha^3}\frac{1}{R}\frac{d}{dt}M_{pq}\left(t-\frac{R}{\alpha}\right) - RP^{far(S)}\frac{1}{4\pi\rho\beta^3}\frac{1}{R}\frac{d}{dt}M_{pq}\left(t-\frac{R}{\beta}\right)$$

where RP^{near} is the radiation pattern in the near field, characterised by $1/R^4$ distance dependence, $RP^{interm(\alpha)}$ and $RP^{interm(\beta)}$ are the radiation patterns for the intermediate field with $1/R^2$ distance dependence; $RP^{far(P)}$ and $RP^{far(S)}$ are the radiation patterns in the far field for P- and S-wave respectively, characterised by 1/R distance dependence. We omit the complete description of the radiation patterns, which are combinations of the directional cosines.

The above equation determines the displacement for the n-th component of the displacement vector caused by the action of a double couple of magnitude M at the source (moment tensor M is assumed to be constant over the source area, which has small linear dimension in comparison to radiated wavelength).

Fig.3-7 shows schematically the distance dependence of the radiated displacement for both radial and transverse components of intermediate and far fields, ignoring the contribution of the near field.

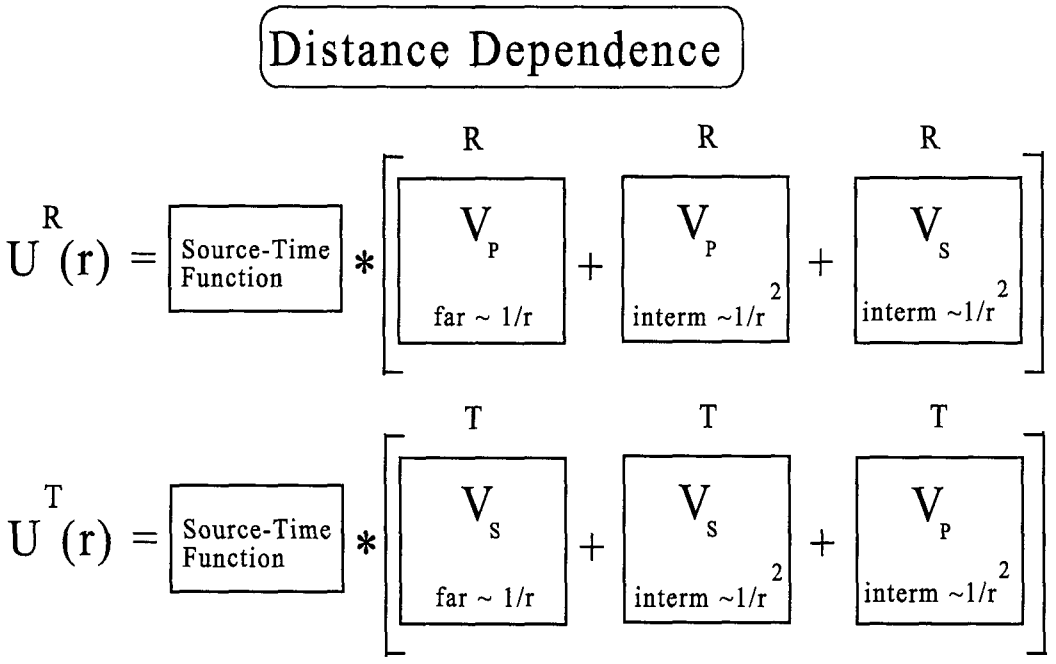

Fig.3-7 Schematic distance dependence of the radiated displacement for the longitudinal (R) and transverse (T) components, including intermediate and far field contributions.

The frequency dependence of the radiated displacement is shown in Fig. 3-8. It should be pointed out that the contribution of the intermediate field to the total displacement is comparable to the far field contribution only in the immediate vicinity of the source. It can be quite significant in the case of seismic monitoring in mines, when seismic stations can be situated very close to the source.

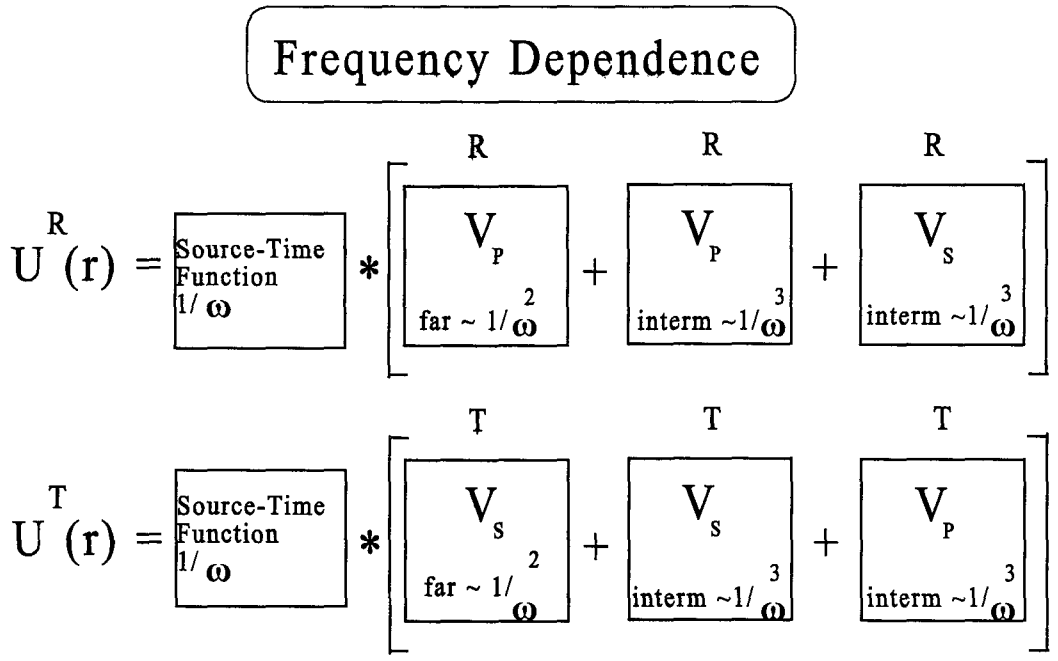

Fig.3-8. Schematic frequency dependence of the radiated displacement for the longitudinal (R) and transverse (T) components, including intermediate and far-field contributions.

From the last equation, it can be observed that in the intermediate field the radiated seismic field at time t depends on the instant value of moment $M(\tau)$ (as shown in Fig.3.9), while the far field radiation depends on the instantaneous *time derivative* at the time $\tau = t - R/v$, where $v = \alpha$ for P-waves, and $v = \beta$ for S-waves.

The intermediate field contributions to the total displacement and velocity wavefield for a source at different distances are shown on Fig.3-10, 3-11.

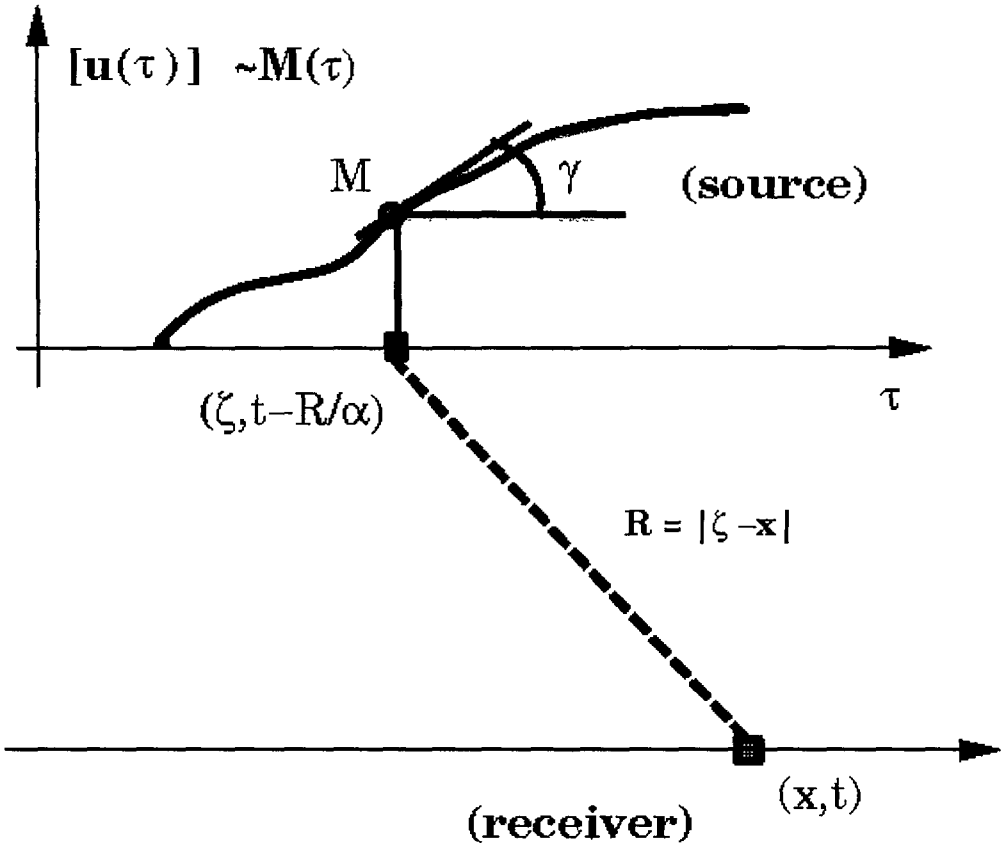

Fig.3-9 In the intermediate field at the point *x* at time *t*, the value of the jump of displacement responsible for the intermediate field at this point is the value of the jump of displacement at the source at the point ζ at time *t* - *R/α*. For the far field the derivative at the same point at the same time is proportional to the far field displacement recorded at point *x* at time *t*.

In order to estimate the relative significance of the intermediate field we have shown on Fig.3-12 and Fig. 3-13 far field contributions to the total displacement and velocity wavefield at the same distances from the same source. As can be expected, the intermediate field contribution quickly diminishes with the distance from the source.

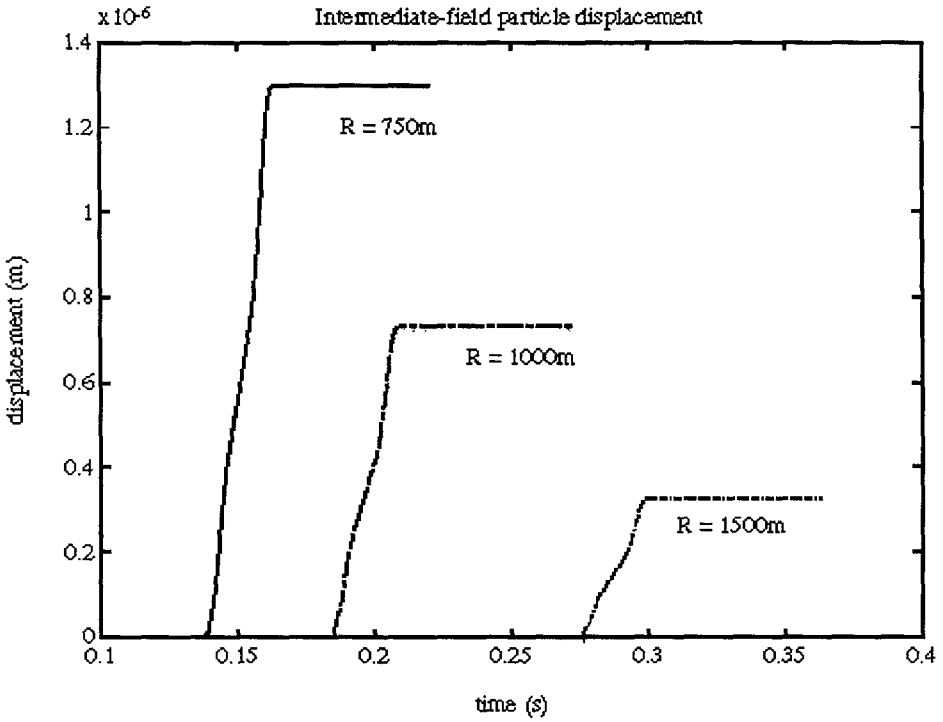

Fig.3-10. Intermediate field particle displacement at different distances from the source.

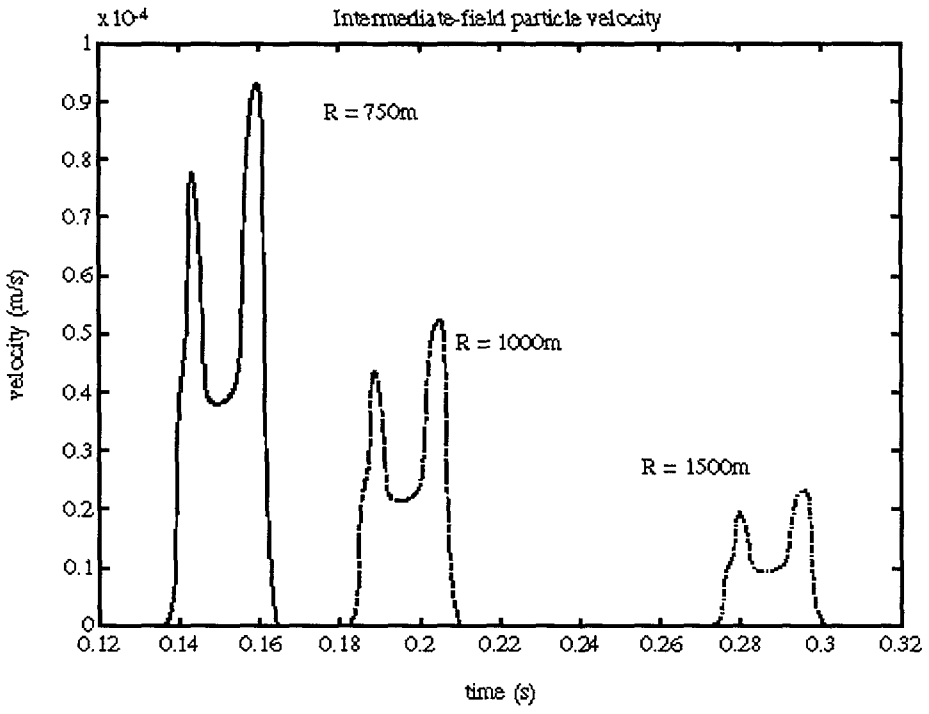

Fig.3-11 Intermediate field particle velocities at different distances from the source.

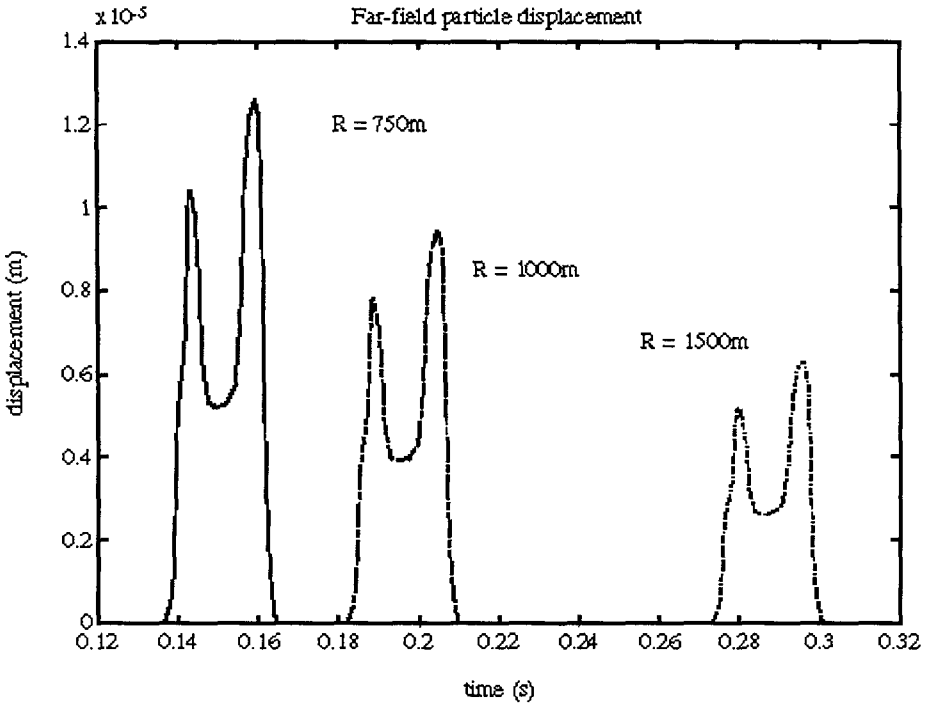

Fig.3-12 Far field particle displacement at different distances from the source.

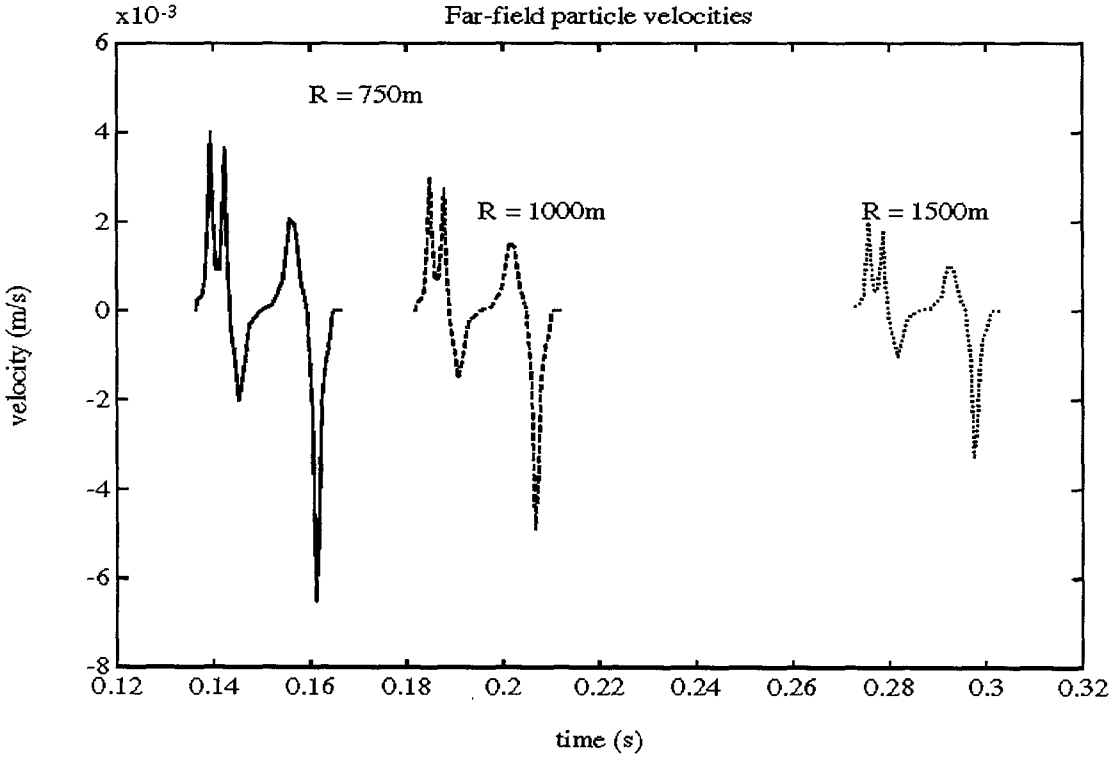

Fig.3-13 Far field particle velocities at different distances from the source.

Let us now consider seismic recordings, obtained in the near vicinity of a seismic source and compare them to the recordings obtained in the far field.

Fig. 3-14 shows a three component velocity seismogram of a seismic event which occurred on 11 Dec 1996 and was recorded at a distance of 450 m. Fig. 3-15 shows the displacement recording, obtained by instrument response deconvolution and integration in the time domain of the velocity seismograms of Fig.3-14. In Figs.3-16 and 3-17, velocity and displacement time histories respectively, for the same event recorded at a distance 1457 m are shown. Comparison of these time histories proves that in the intermediate field there is no clear P- or S-wave arrival, as predicted by the previous equation. It is also obvious that seismograms recorded in the near/intermediate field contain much lower frequency components compared to the seismograms in the far field.

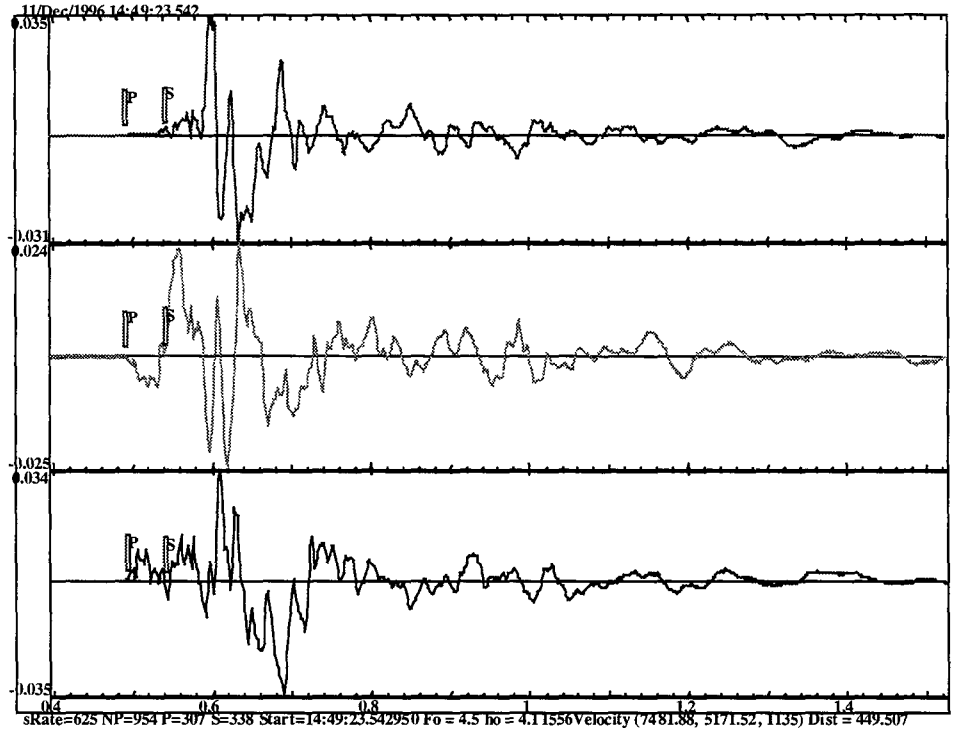

Fig.3-14 The three component velocity seismograms of a seismic event recorded in the intermediate field.

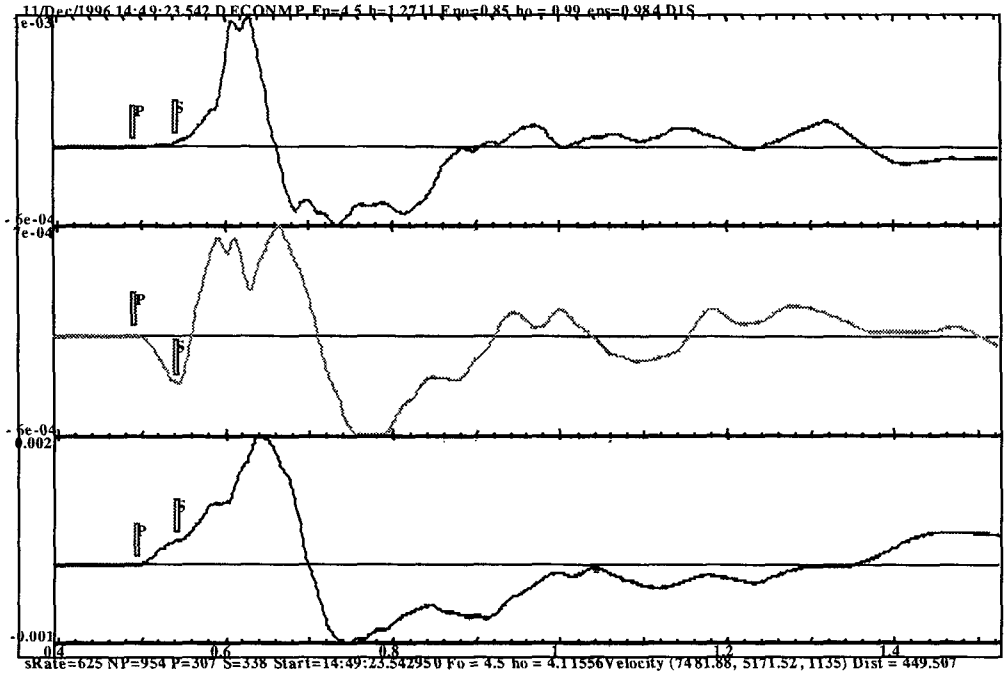

Fig.3-15 The three component displacement seismograms obtained by instrument deconvolution and integration of the velocity seismograms recorded in the intermediate field, shown in Fig.3-4.

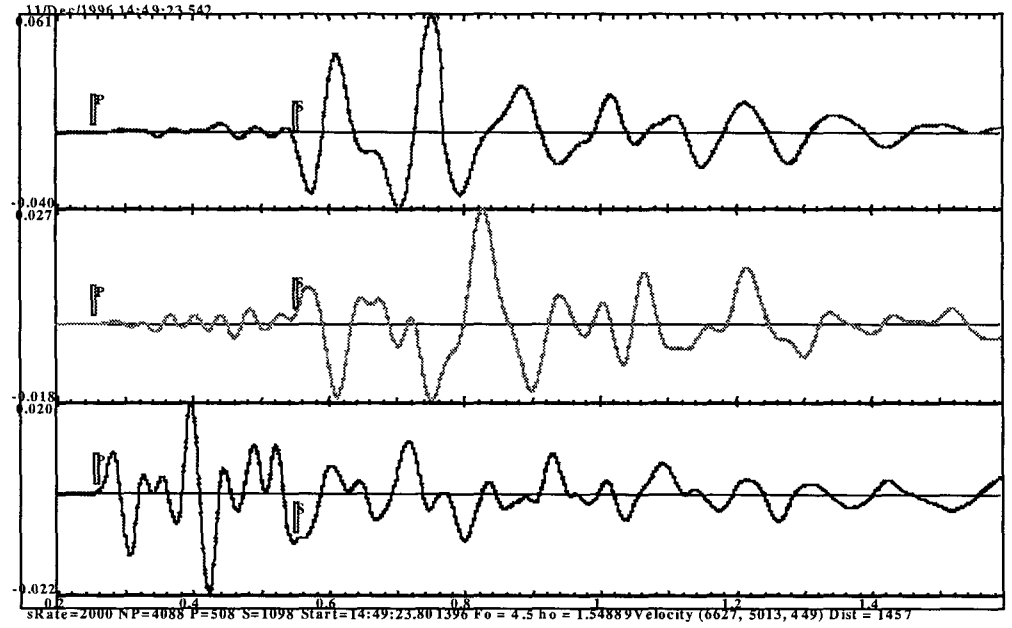

Fig.3-16 The three component velocity seismograms of the seismic event recorded in the far-field.

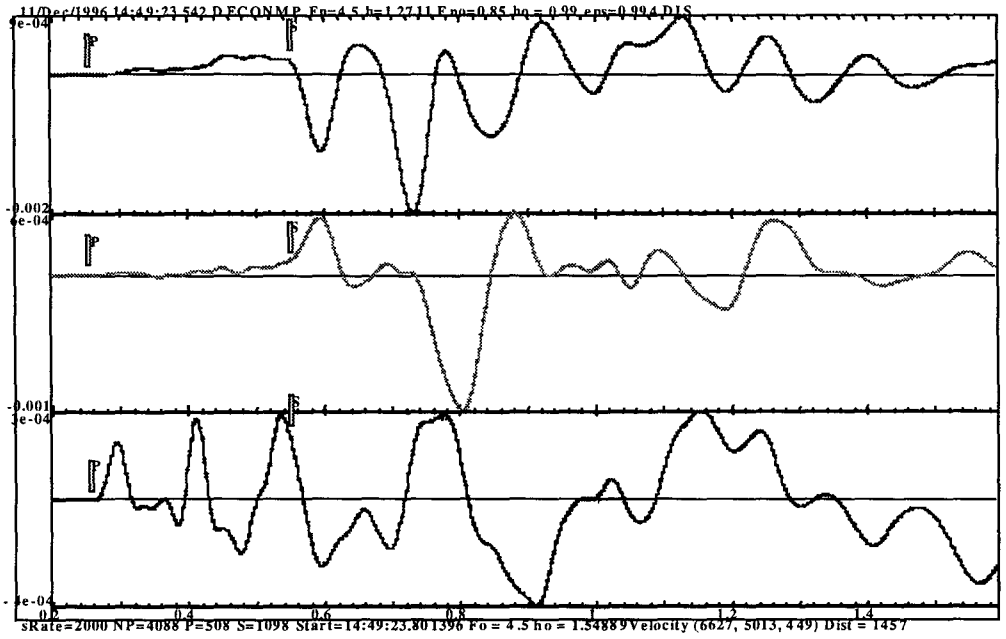

Fig.3-17 The three component displacement seismograms obtained by the instrument response deconvolution and integration of the velocity seismograms obtained in the far field shown in Fig. 3-16.

This property can be utilised if we are to use Brune's model with seismic receivers situated in intermediate field. High-pass filtering may be applied prior to spectral estimation followed by the application of intermediate field correction coefficients. In the following we will show an example of the application of the described processing to the special cluster seismic network.

3.4 Case studies using special cluster network.

For the case studies we have used data recorded by an ISS micronetwork, which has been developed as part of the IASPEI (International Association of Seismology and Physics of the Earth's Interior) semi-controlled seismic experiment by Kyoto University, BPI (Bernard Price Institute) of Wits University, ISS International and Western Deep Levels South Mine. This seismic network consists of accelerometers only, providing high-quality seismic records in the near, intermediate and far fields. Due to the closeness of the seismic source, seismograms recorded by this network have a very complicated form. A time domain integration procedure has been applied to the acceleration recordings, prior fitting Brune's model. It should be pointed out that the widely used integration in the

frequency domain, does not lead to satisfactory results due to low signal to noise ratio in the low-frequency region, and the need to integrate twice in order to convert acceleration spectra to displacement spectra.

In Fig 3-18 such displacement spectra integrated in frequency domain and corrected for geometrical spreading and Q are shown.

Example of a such source inversion based on the double time domain integration procedure followed by the application of multitaper spectral estimation technique is shown in Fig.3-19.

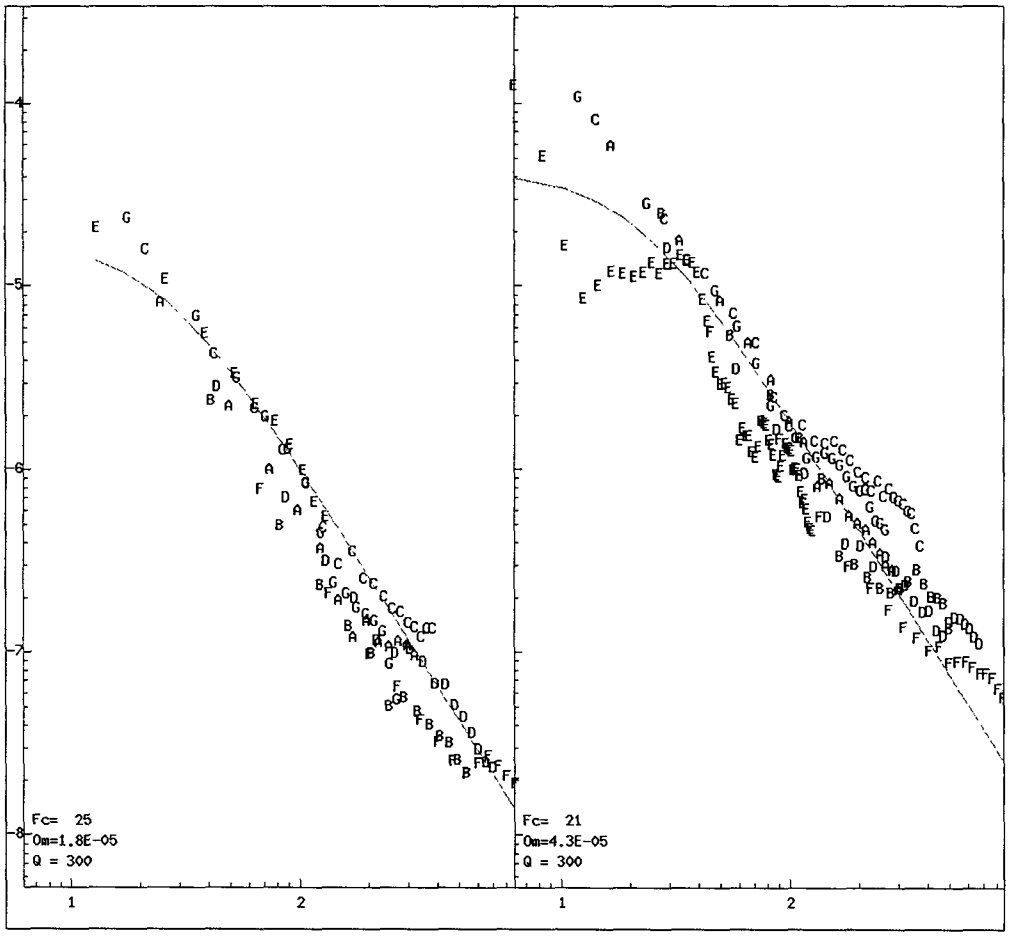

Fig.3-18 Amplitude spectra of P and S waves for seven stations for an event with magnitude 1.2, recorded by the special cluster network. The spectra have been corrected for geometrical spreading and Q, but without corrections for the intermediate field and using spectral domain integration. The results of source parameter inversion are also shown in the left bottom corner of each spectral stack. Units along the horizontal axis are shown as powers of 10 Hz, on the vertical axis in powers of 10 m*s.

Comparison of Fig 3-18 and Fig.3-19 shows that without proper corrections for the intermediate field, estimates of corner frequency and Q can be quite wrong. The problems with double spectral domain integration from acceleration recordings to displacement are most noticeable in the low frequency range, making the estimate of seismic moment difficult.

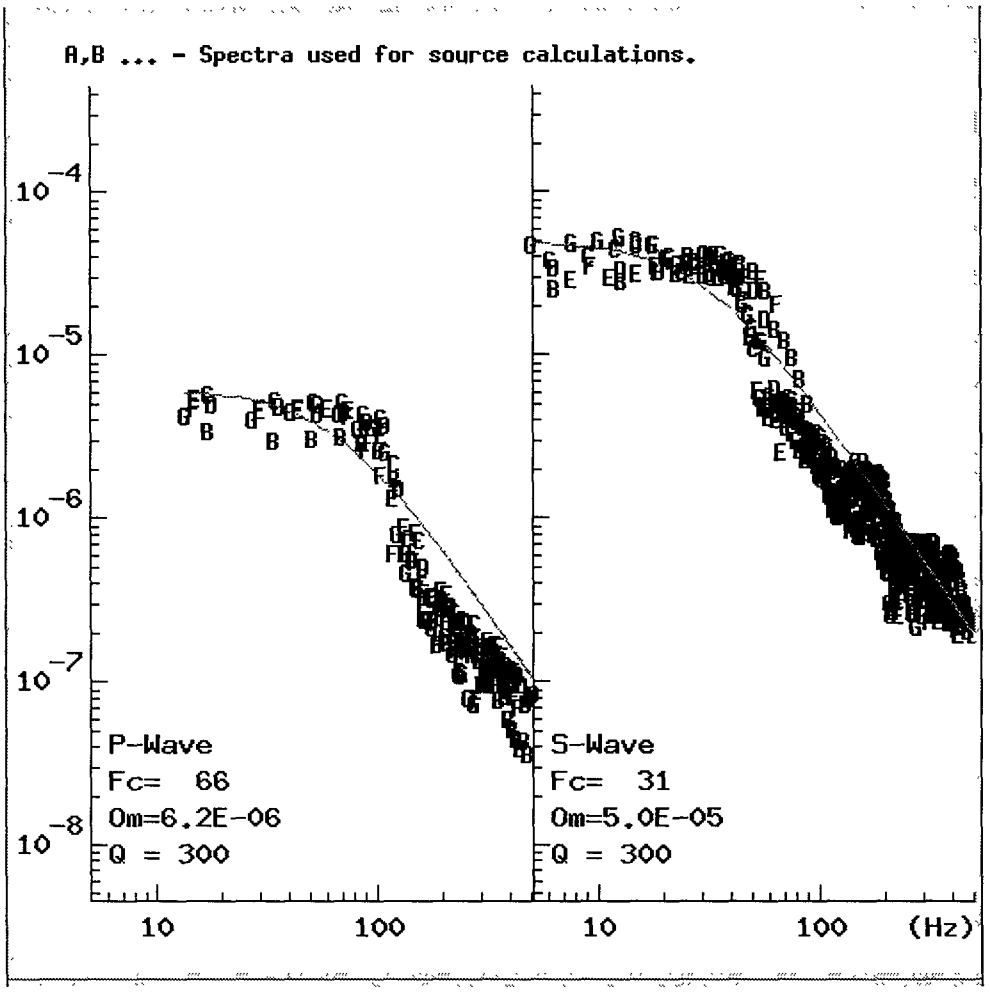

Fig.3- 19 Displacement spectra of P and S waves for the same event as shown in Fig. 3-18. The spectra have been corrected for geometrical spreading and Q. The results of source parameter estimation are also shown. Units on the vertical axis are m*s, on the horizontal axes are in Hz. Raw recordings have been integrated twice using a specially developed time domain integration procedure.

Several hundreds seismic events have been processed using the time domain integration procedure and intermediate field corrections. Results obtained indicate improved fit of calculated spectra to the Brune model.

(57 m) to the seismic source. The contribution of intermediate field has more of a low frequency content, and this property may be employed for the inversion of seismic records in the intermediate and near fields, using far-field Green's functions.

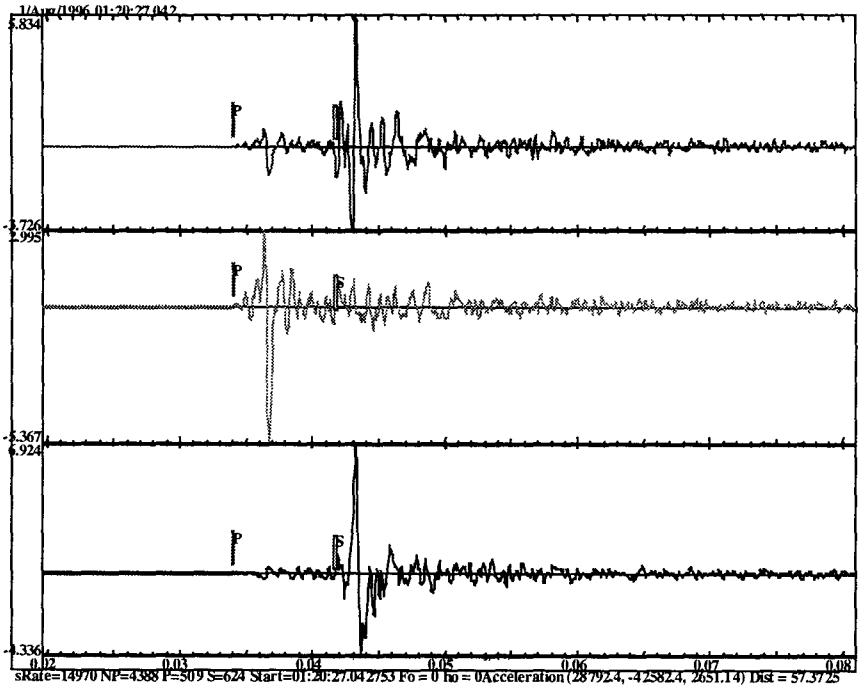

a).

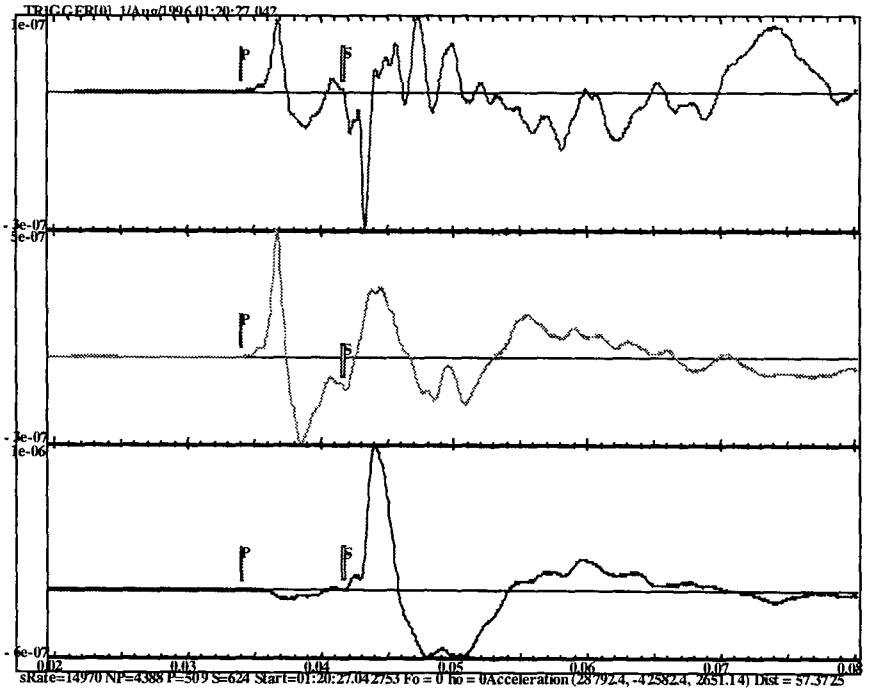

b)

Fig.3-20 a. Acceleration recordings of seismic event of magnitude M = 0.2, recorded at the distance of 57 m from the source. b. Displacement seismograms obtained by double time domain deconvolution of accelerograms, shown in a).

4 Source parameters as a function of time and location of the rupture front.

4.1 Source radiation as seen in the near field and monitoring the propagation of the rupture front

Source parameter inversion in the near/intermediate field is usually carried out using finite difference/element methods. In this case a grid of point dislocations simulates the large (or extended) source. Further, the integrals over the fault surface are replaced by summations of all point sources, and the synthetic seismograms are calculated for each of the point sources using finite difference/element methods. These methods are computationally extremely expensive. To further aggravate the inversion problem, these computations must be repeated at every iteration step. Recently developed new ray-theory based wave propagation algorithms allow fast calculation of far-field synthetics, but they are not generally applicable to the near-field radiation. The usual approach, which was frequently adopted for overcoming the inherent problems of the lack of applicability of ray theory methods to the near-source synthetics, was to ignore the near field contributions. In this case the assumption has been made that the total wavefield can be represented by far-field contributions only, thus *using far-field Green's functions in the near-source region.* But being a high-frequency approximation, ray theory cannot truthfully describe the total wavefield at relatively low frequencies, which is very important for the estimation of source dimensions. Taking into account that at frequency f, the approximate ratio of far-field to near field wave amplitude is $2\pi fR/v$, where v = P or S wave velocity, and R is hypocentral distance, it becomes apparent that ignoring near-field contributions is equivalent to modelling only high-pass frequency filtered near-source seismograms. Simple calculation shows that for the case $R = 200$ *m* and $v = 3500$ km/s the near-field contribution drops to less than 10 per cent of the far-field contribution only in the frequency range above 28 *Hz,*. This represents quite serious problem for source parameter inversion purposes.

It has been recently shown (Joyner and Spudich, 1994) that for a uniform whole space the various terms in the Green's function can be transformed into sums of nondispersive pulses. In this case the contributions of the far, intermediate and near fields can be calculated directly in the time domain, and the total wavefield can be represented as a sum of all above terms. Advantages of such an approach are obvious:

- We can use isochron formalism, which proved to be very efficient for computing synthetic seismograms using far-field ray-theory Green's functions for finite fault radiation problems (Bernard and Madariaga, 1984, Spudich and Frazer, 1984), and still retain near and intermediate field contributions.
- The isochron integration technique proved to be helpful for gaining insight into the fine structure of the source processes and can explain many peculiarities of the near-source range waveform behaviour.

The proposed algorithm for producing synthetic seismograms is based on ray theory. It combines the isochron integration method in the vicinity of the source for computation of far, intermediate and near field contributions and the powerful recursive cell raytracing (or another type of wavefront construction waveform modelling) for far-field synthetics at some distance from the source. In the vicinity of the source, the geological medium is assumed to be homogeneous and isotropic, while for the far-field approximation almost any arbitrarily complex three-dimensional geological medium model can be used.

The isochron method uses ray theory, so the latest developments in that field can be used to allow arbitrary complex media models with smooth interfaces to be used for source radiation computation in both the near and the far field. We used the wavefront construction method (Vinje, et al. 1993) and the recursive cell ray-tracing method (Moser and Pajchel, 1996). In the vicinity of the source, assuming smooth lateral velocity model variations the use the wavefront construction method is proposed due to the simplicity of this method compared to the recursive cell. Both methods require as input the initial wavefront to be propagated. This initial wavefront is calculated using the isochron method, separately for P and S waves. Once this wavefront is constructed it is propagated throughout the whole model space subject to some configurable restrictions (e.g. the number of multiple reflections per layer, inclusion of diffraction, etc.). Both methods can handle caustic points encountered by seismic rays. Below we briefly describe the algorithm and show some examples for the Haskell source model.

4.1.1 Algorithm for near field synthetic calculations using isochron method.

1. Input information required:

- Source plane dimensions and geometry: strike, dip, dimensions. Initially, only rectangular shape fault geometry is considered, although the extensions of the proposed algorithm to other source geometry configurations are straightforward.
- Rupture time distribution on the source plane. It must be specified on some two-dimensional grid along the fault surface. This is the grid on which the initial fault rectangle is subdivided for further calculations.
- We assume that the same "ramp-like" slip time history function is applicable for each point of the source plane:

$$\Delta u(\bar{r}_0, t) = \begin{cases} 0, & 0 < t < t_r(r_0) \\ (t - t_r)\, D_0/\tau, & t_r(r_0) < t < t_r(r_0) + \tau \\ D_0, & t > t_r(r_0) + \tau \end{cases} \qquad (4.1)$$

where $\Delta u(\bar{r}_0, t)$ is the scalar slip function, D_0 is the final dislocation at the point r_0; t_r is the rupture time; τ is the rise time. Generally, values of D_0 and τ may vary from point to point on the source surface, but initially we can assume that they are the same for all points. It must be pointed out that the time derivative of the scalar slip function shown above is a simple boxcar function, with amplitude equal to D_0/τ and a width τ.

- For a layered medium the far field Green's function may be written in the general form [Farra et al., 1986]

$$G^{FF}(\bar{r}_o, t) = \frac{\mu_o}{4\pi\rho_o c_o^3} Re\left[\sqrt{\frac{\rho_o c_o}{\rho c J}}\, \boldsymbol{F}_c \prod \Delta(t - T^c)\right] \qquad (4.2)$$

where μ_o, ρ_o, c_o are the rigidity, the density and the wave velocity evaluated at the source, respectively. $\boldsymbol{F}_c$ is the radiation pattern vector, J is the geometrical spreading, and Π contains the product of all complex transmission coefficients at the different interfaces encountered by the direct ray along its travel path.

$\Delta(t) = \delta(t) - i(\pi t)^{-1}$ is the analytical function, which corresponds to the Dirac's delta function. In order to avoid numerical instability problems when evaluating the far-field Green's function Madariaga and Papadimitriu, 1985, and Farra et al., 1986, replaced $\delta(t)$ with the analytical function $S(t) = -\frac{i}{\pi}\frac{1}{t - i\Delta t}$, which approaches to the analytic delta function when $\Delta t \to 0$. This function acts like a filter by reducing the spectral amplitudes for frequencies greater than $1/\Delta t$. For a more complicated geological medium one can use recursive cell ray-tracing techniques or the wavefront construction method, instead of using simplified Green's function like (4.2).

- The effect of anelastic attenuation can be included by the convolution in the frequency domain of the Green's function with the constant Q attenuation function defined by [Carpenter, 1966]:

$$Q(f,t^*) = \exp\left[-\pi f \frac{t^*}{2} - i\,2\pi f t^* \ln\left(\frac{f}{f_N}\right)\right], \qquad (4.3)$$

where $t^* = T_c/Q$, T_c is the body wave travel time, Q is the constant "quality factor", f is the frequency, and f_N - Nyquist frequency.

4.1.2 Ray theoretical strong ground motion modelling

Now we will formulate initial conditions and outline the strategy of synthetic seismogram calculations.

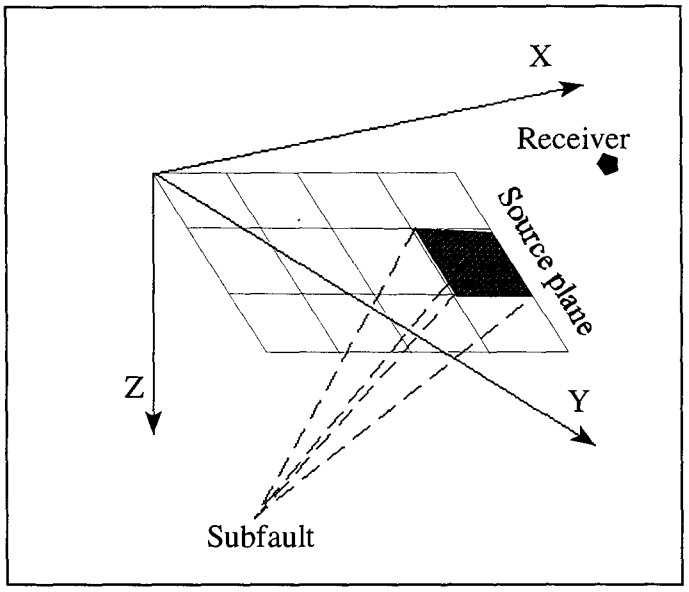

Fig. 4-1. Fault geometry and source parameterisation.

- The source is divided into several equal size rectangular subfaults (Fig.4-1). The slip at each subfault is specified by the ramp-like function (4.1). Let us assume that the size of each elementary subfault is Δx by Δy, and M and N are the numbers of subfaults in the X and Y directions respectively.
- Modelling assumes that the rupture times, the final dislocation values and the rise times are specified for every grid point, i.e. at the subfault corners. For every receiver location it is necessary to calculate the traveltimes from the receiver position to the subfault corners.

- Then isochron times can be obtained by summing rupture times and traveltimes from the receiver to the subfault corners. For isotropic, homogeneous media simple Green's functions like (4.2) can be used. For more complicated geological media one can use wavefront construction/recursive cell ray-tracing methods. But this is only applicable to the far-field P and S waves contribution only. For the isotropic and homogeneous media and for the receivers in the near- or/and intermediate field we can use simple (or relatively simple) relations from Joyner and Spudich (1994) which are discussed below. Once isochron times are known at the subfault corners, then the isochron times at any point of the subfault element *(m,n)* are obtained by the interpolation formula(Yoshida,1986):

$$t(x,y) = \frac{1}{\Delta x \Delta y}\,[(\Delta x - x)(\Delta y - y)T_{m,n} + (\Delta x - x)yT_{m,n+1} + (\Delta y - y)xT_{m+1,n} + xyT_{m+1,n+1}] \qquad (4.4)$$

where $T_{i,j}$, $(i = m, m+1;\ j = n, n+1)$ are the isochron times at the subfault corners.

- The subfault dimensions are considered to be small enough, so that the direction cosines and geometrical spreading do not vary over subfault surfaces, i.e. *the Fraunhofer approximation is applied at the subfault scale.* This implies that the propagation effects on pulses radiated from any point on the subfault are approximately the same and that they can be described by a representative subfault Green's function computed for the ray leaving the middle point by using equation (4.2). Then, using this approximation, we can write the representation integral for a discretized source plane: $u^c(r,t) = \sum m,n\, u^c_{m,n}(r,t)$, (4.5)

where $\mathbf{u}^c_{m,n}(r,t) = G^{FF}_{m,n} \otimes \int_{subfault} \Delta\mathbf{u}^{m,n}(r_o^{m,n}, t - T_c^{m,n})\, d\Sigma$ (4.6)

For a given time t and a boxcar slip velocity function (i.e. "ramp-like" slip function) the subfault regions S_o, where the slip velocity is not vanishing is bounded by isochrons $L_t = x(t,y)$ and $L_{t-\tau} = x(t-\tau, y)$ and the edges of the subfault.

4.1.3 An example of application to the Haskell source model.

The Haskell model of rupture occurring in a uniform whole space is used here to illustrate the basic principles of the synthetic seismogram computation procedure. The geometry of the Haskell model is shown in Figure 3.2.

The rupture starts at the hypocentre and propagates with constant rupture velocity until it reaches the boundaries of the source model on the fault plane. Maximum dislocation is

assumed to be uniform over the whole source surface, as are the rise times and rake. Later it will be shown how these restrictions can be easily overcome.

Following the pioneering papers by Bernard and Madariaga (1984) and Spudich and Frazer (1984) isochron distributions for both P and S waves have been calculated prior to numerical integration along the fault surface. Isochrons for P and S waves for the chosen position of the receiver (specified in Fig. 4.2) are shown in Fig. 4.6 and 4.7 respectively. It should be pointed out that although the rupture velocity distribution does not depend on the position of the observer, the isochron distribution varies with the position of the receiver. This follows from the definition of the isochrons as the sum of the rupture times and the travel times from the chosen fault plane point to the receiver.

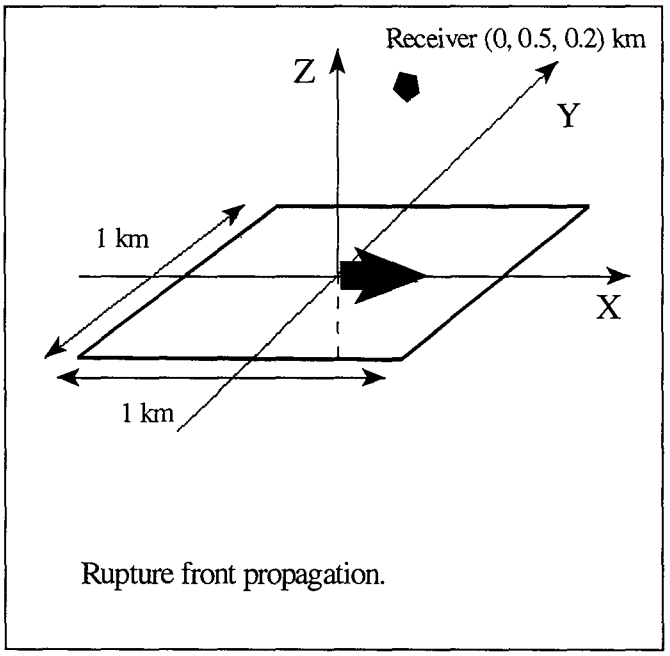

Fig. 4.2 Geometry of the source and receiver location for a Haskell model in the whole space. Dimensions of the source are 1km x 1km, and it lies in the XY plane. The rupture front is a line parallel to the Y-axis and advances in the positive X direction. The receiver is situated at the position (0, 0.5, 0.2) km.

In Fig.4-3 (a,b) the far field P and S wave velocity seismograms are shown, while in Fig.4-4(a,b) P and S wave intermediate field contributions to the total wavefield for the same position of receiver are plotted.

As has been pointed out earlier, near field P and S wave contributions cannot be separated.

A breakdown for the total far, intermediate and near field contributions is shown in Fig.4.5. Close examination of Fig.4.3 through Fig.4.5 clearly demonstrate that the total wavefield is mostly composed of S-waves (except the near field case, where it is impossible to separate P and S waves), the maximal amplitude of which exceeds that of P wave by almost an order of magnitude. Analysis of the polarisation of P and S waves shows that the motion is not rectilinear, even in this simplest case of first arrivals and a homogeneous isotropic medium.

It should be emphasised that the seismograms shown below have been obtained directly in the time domain, using a fast and extremely efficient isochron integration technique. In Fig. 4.8 and Fig. 4.9 isochron distributions, for P and S waves respectively, are shown for the position of receiver and model parameters specified in the caption to Fig. 4-3. The source, 1 km x 1 km in size, has been subdivided into 50x50 rectangular subfaults, each of which in turn has been subdivided into two triangles. Subdivision of the whole source into a large number of triangles significantly reduces the computational burden for the calculation of Green's functions. We can assume the Fraunhofer approximation at triangular or even rectangular level and precalculate Green's function for the given position of the receiver and for each of the rectangles composing the source. Therefore, when applying this type of modelling for inversion purposes, one can simply use precalculated Green's functions for every iteration.

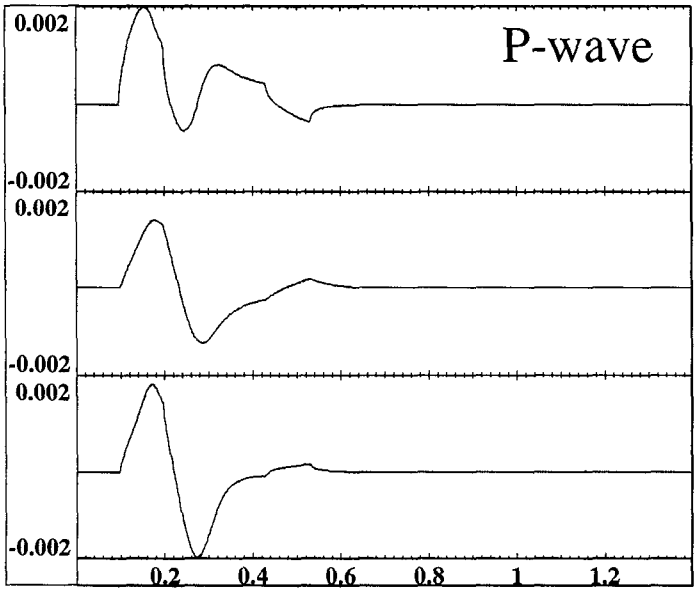

Fig. 4.3a,

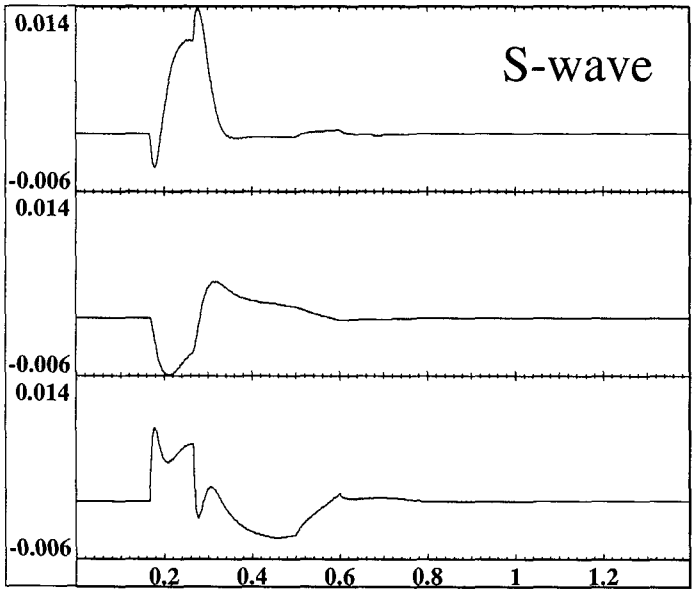

Fig. 4.3b Far field P and S wave velocity seismograms for a Haskell model. They have been calculated for the receiver position (0, 0.5, 0.2) km, using a ramp-like slip function with the following parameters: slip velocity 1.0 cm/sec, rise time 0.1 sec, α = 6.0 km/sec, β = 3.4 km sec, ρ = 2.5 g/cm^3, rupture velocity 3.0 km/sec. Vertical units are m/sec, while horizontal are sec.

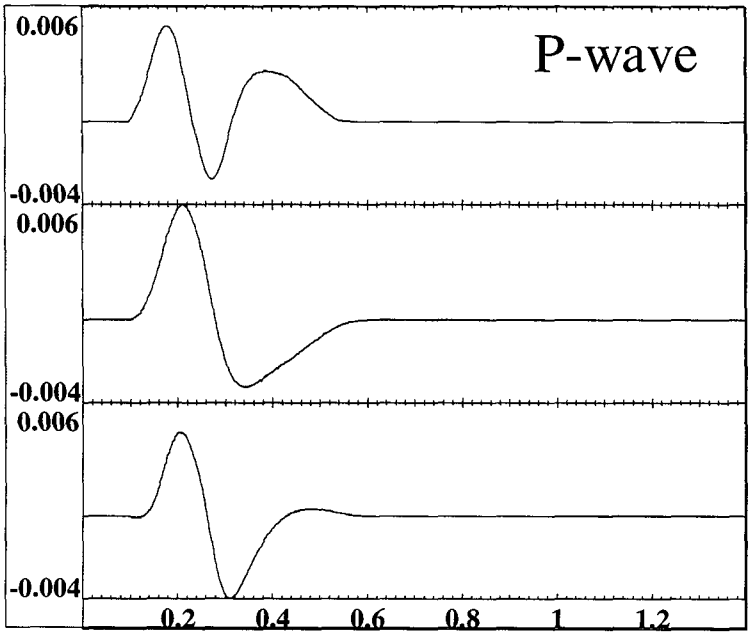

Fig. 4-4a,

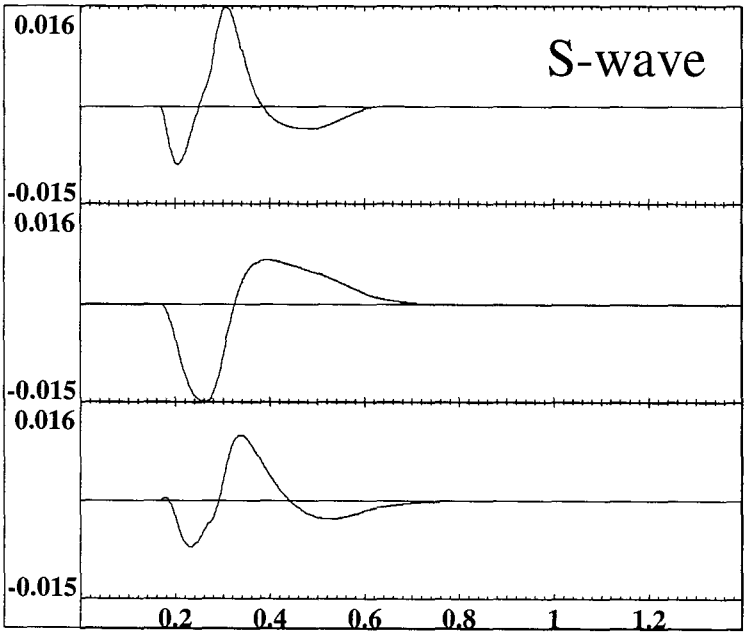

Fig. 4-4b Intermediate field P and S wave velocity seismograms for a Haskell model. For details see caption to the previous Figure.

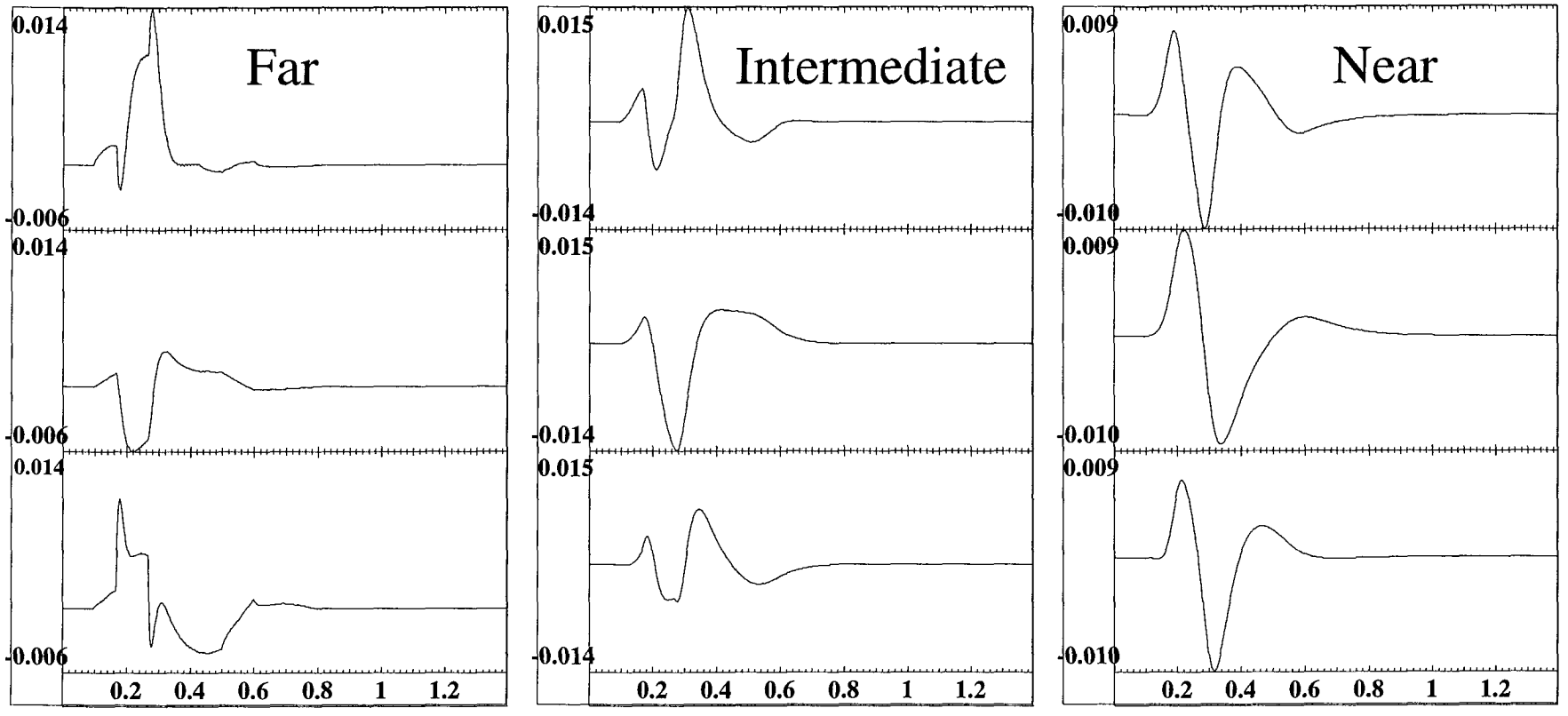

Fig. 4-5 Total far, intermediate and near field contributions calculated for the same Haskell model as shown in Fig. 4-2. For details see caption to Fig.4-3.

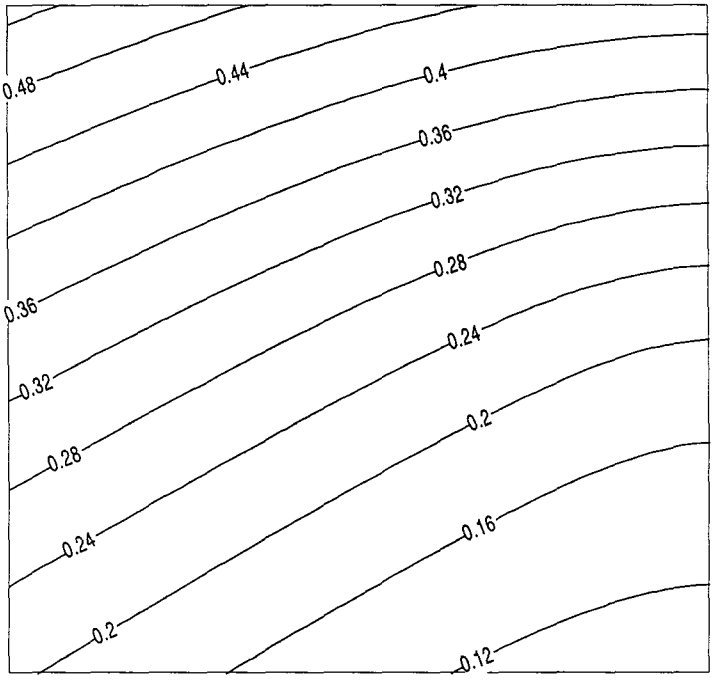

Fig.4-6 P wave isochrons for the source and receiver geometry shown in Fig.4-2. For details see the caption to the Fig.4-3. In order to obtain the value of displacement at certain time t_o one must carry out integration not over the entire source plane, but over the isochron $t = t_o$, thereby reducing the surface integral to a line integral.

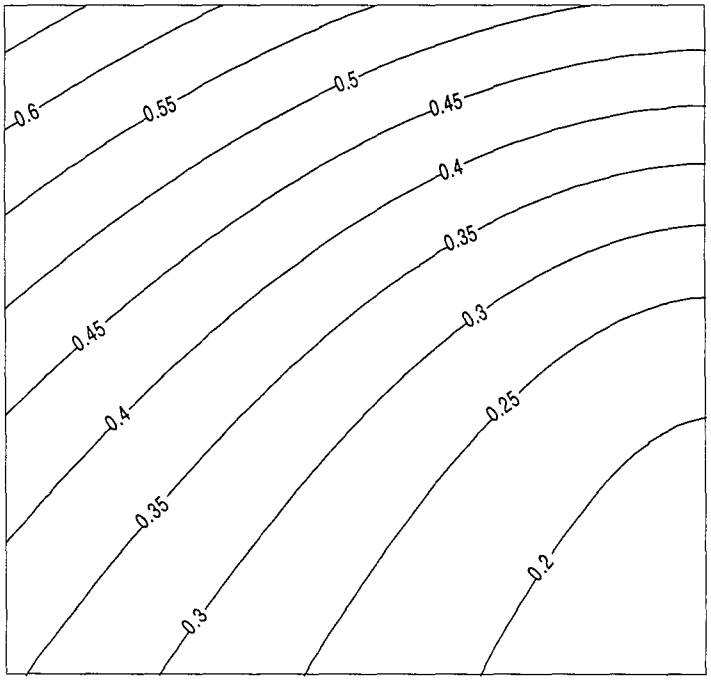

Fig. 4-7 Isochrons of the S wave. For details see the caption the Fig. 4-6.

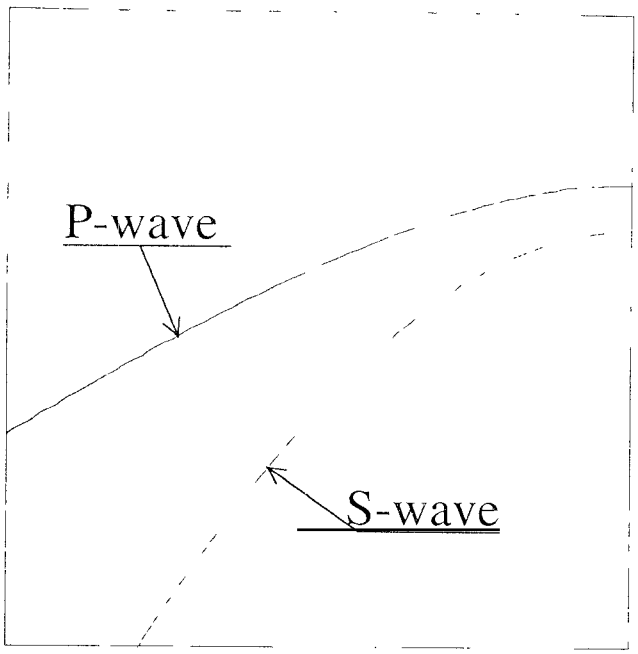

Fig. 4-8. Integration paths for the $t = 0.3$ s isochron for the P and S waves.

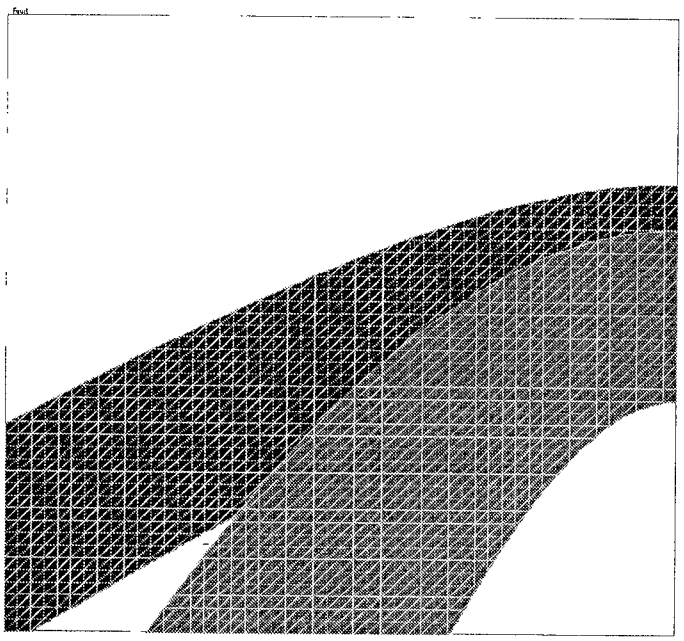

Fig. 4-9 Integration strips for the model and the receiver location described in the caption to Fig. 4-3 with the assumption of a "ramp-like" slip function, rise time $\tau = 0.1$ s for the time $t = 0.3$s. These strips, shown separately for P and S waves, representing regions of nonzero contribution to the displacement seismograms, are regions restricted by the isochrons t = 0.3s and t = 0.3 - τ. Rise time is assumed to be the same for all subfaults taking part in the integration procedure. See text for explanation. The 50 x 50 rectangular grid used is shown by the lighter lines.

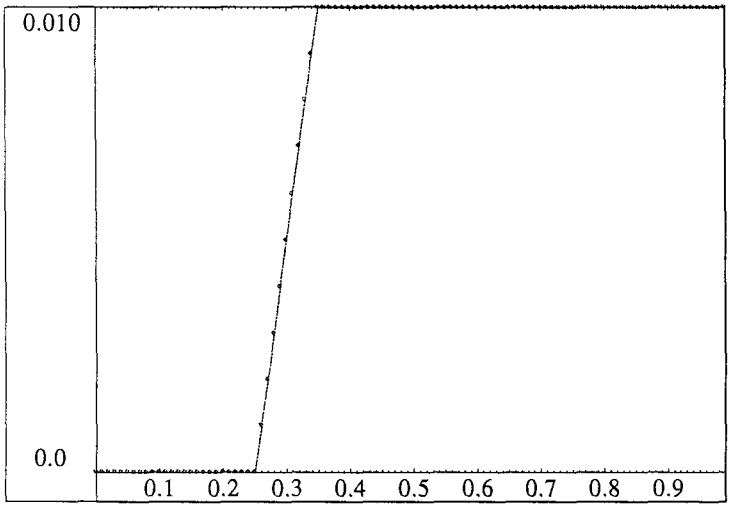

Fig. 4-10 Slip time history used throughout current report, with rise time τ = 0.1 s, D_o=0.01 m.

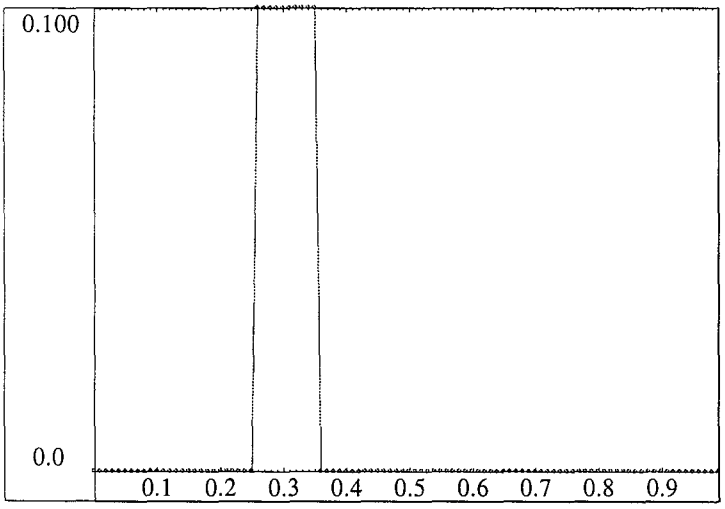

Fig. 4-11 Slip velocity function for the model in Fig. 4-11. For the "ramp-like" function the slip velocity is simple boxcar function.

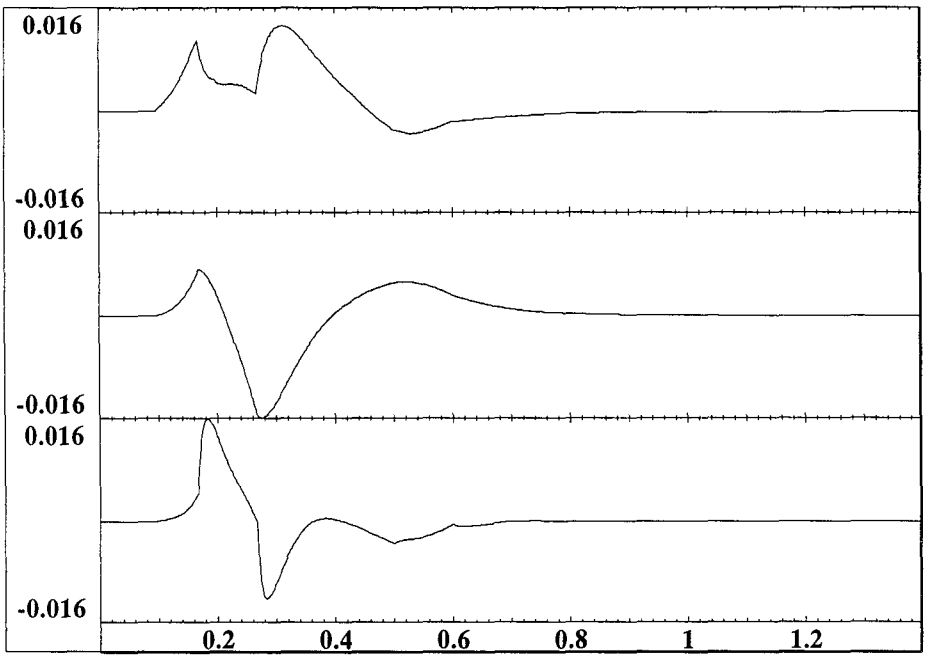

Fig. 4-12 Complete velocity synthetic seismograms for the receiver at (0, 0.5, 0.2) km including far, intermediate and near fields.

4.2 Reconstruction of the source time function for different parts of the rupture.

Far field contributions of a finite source to the total acceleration wavefield can be evaluated using the following equations (Joyner & Spudich, 1994):

$$\frac{\partial^2 \mathbf{u}^N(x,t)}{\partial t^2} = \frac{\mu}{4\pi\rho}\left[\int_{-\infty}^{+\infty} d\tau \frac{d}{dt} h(t-\tau)\left(\int_{t_\alpha+t_r=\tau} dl \frac{D_0\, t_\alpha\, \mathbf{A}^N}{r^4|\nabla\tau|} - \int_{t_\beta+t_r=\tau} dl \frac{D_0\, t_\beta\, \mathbf{A}^N}{r^4|\nabla\tau|}\right) + \int_{-\infty}^{+\infty} d\tau\, h(t-\tau)\left(\int_{t_\alpha+t_r=\tau} dl \frac{D_0\, \mathbf{A}^N}{r^4|\nabla\tau|} - \int_{t_\alpha+t_r=\tau} dl \frac{D_0\, \mathbf{A}^N}{r^4|\nabla\tau|}\right)\right]$$

$$\frac{\partial^2 \mathbf{u}^{IP}(x,t)}{\partial t^2} = \frac{\mu}{4\pi\rho\,\alpha^2}\int_{-\infty}^{+\infty} d\tau \frac{d^2}{dt^2} h(t-\tau) \int_{t_\alpha+t_r=\tau} dl \frac{D_0\, \mathbf{A}^{IP}}{r^2|\nabla\tau|}$$

$$\frac{\partial^2 \mathbf{u}^{IS}(x,t)}{\partial t^2} = \frac{\mu}{4\pi\rho\,\beta^2}\int_{-\infty}^{+\infty} d\tau \frac{d^2}{dt^2} h(t-\tau) \int_{t_\beta+t_r=\tau} dl \frac{D_0\, \mathbf{A}^{IS}}{r^2|\nabla\tau|}$$

$$\frac{\partial^2 \mathbf{u}^{FP}(x,t)}{\partial t^2} = \frac{\mu}{4\pi\rho\,\alpha^3}\int_{-\infty}^{+\infty} d\tau \frac{d^3}{dt^3} h(t-\tau) \int_{t_\alpha+t_r=\tau} dl \frac{D_0\, \mathbf{A}^{FP}}{r|\nabla\tau|}$$

$$\frac{\partial^2 \mathbf{u}^{FS}(x,t)}{\partial t^2} = \frac{\mu}{4\pi\rho\,\beta^3}\int_{-\infty}^{+\infty} d\tau \frac{d^3}{dt^3} h(t-\tau) \int_{t_\beta+t_r=\tau} dl \frac{D_0\, \mathbf{A}^{FS}}{r|\nabla\tau|} \qquad (4.7)$$

where $\boldsymbol{u}^N, \boldsymbol{u}^{IP}, \boldsymbol{u}^{IS}, \boldsymbol{u}^{FP}, \boldsymbol{u}^{FS}$ are the near, intermediate P, intermediate S, far P and far S field displacements respectively, $\boldsymbol{A}^N, \boldsymbol{A}^{IP}, \boldsymbol{A}^{IS}, \boldsymbol{A}^{FP}, \boldsymbol{A}^{FS}$ are the near, intermediate P, intermediate S, far P and far S radiation patterns, $h(t - \tau)$ is the slip time history, which is assumed to be the same along the source surface, but normalised by its maximum value, D_0 is the final dislocation, which may vary along the source surface, $|\nabla \tau|$ is the gradient of τ . The equations $\tau = t_\alpha + t_r$ and $\tau = t_\beta + t_r$ describe a family of isochrons on the rupture surface (*e.g.* see Fig.4-6 and Fig.4-7). As becomes apparent from consideration of the system of equations (4.7) shown above, all of the differential equations require integration along the P and/or S wave isochrons, but each with a different integrand value. It should also be pointed out that using the above approach, contributions of the near, intermediate and far fields could be computed separately for different types of waves, except the near field. The inner integral in system (4.7) is the integral along the isochrons, while the outer integral can easily be recognised as the convolution, which can be calculated using the Fast Fourier Transform algorithm. Using the frequency domain approach for the computation of convolution may also help to alleviate numerical problems arising from the discontinuity of the slip function model defined by equation (4.1), used in Haskell's model (In this case one could use the slip velocity function to calculate the Fourier Transform (FT) to obtain a value of $\frac{\partial h(t)}{\partial t}$ and then in order to obtain the FT of $h(t)$, division in the frequency domain by $i2\pi f$ could be used for all f not equal to zero).

4.3 Calculation of source parameters as a function of time and location on the rupture front

In this section applicability of equation (4.7) to the problem of source parameter calculation will be discussed. This will be done using Haskell model example described in section 4.1.3.

In Fig. 4-13 through Fig. 4-15 the intermediate field P, S wave, and total wavefield are shown for the same model, details of which are described in Fig.4-3. Please note, that in that case, in order to obtain intermediate field contributions integration has been carried out using the same isochrons as shown in Fig.4-7 and Fig.4-8 for P- and S-waves separately.

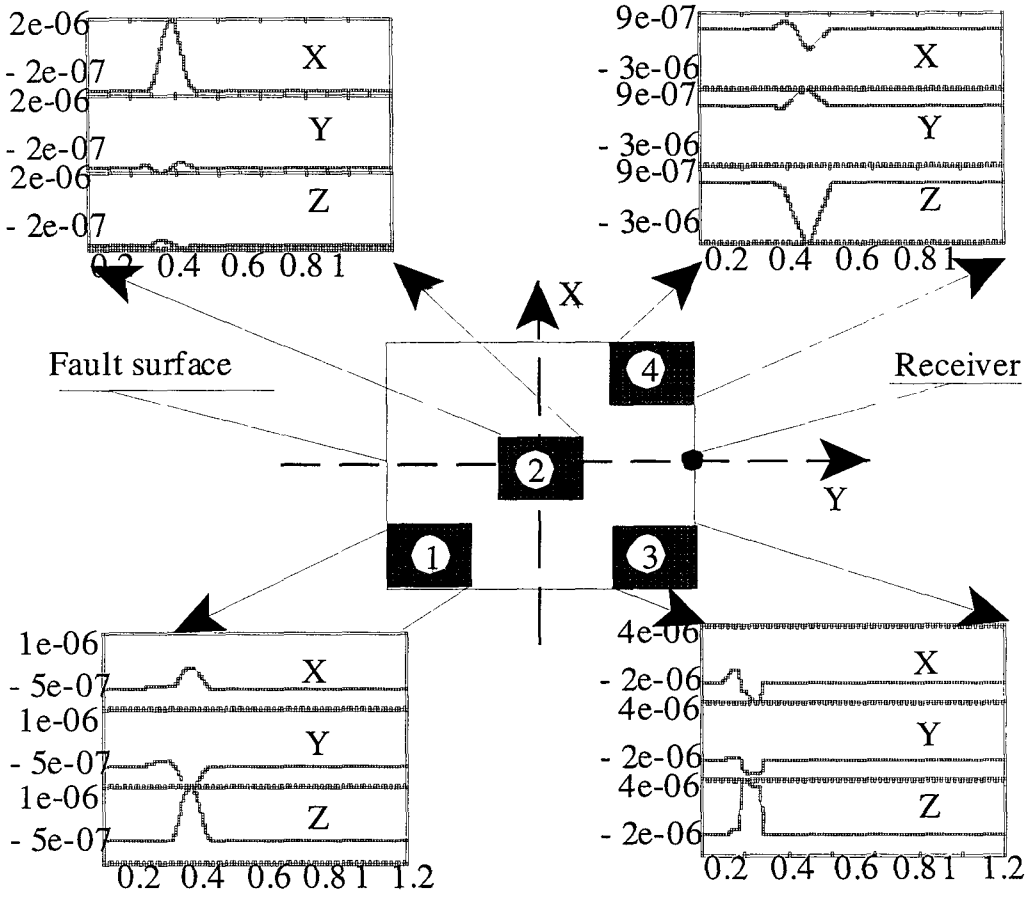

Fig. 4-14 Contributions of different parts of the rupture front to the total far field displacement wavefield. Projection of the receiver position onto the source surface is shown as a filled circle. The vertical units on displacement seismograms are m, while the horizontal units are s. For details of the source model and the receiver geometry see the caption to Fig. 4-3.

After every individual component of acceleration is computed according to equation (4.7), then the total acceleration can be evaluated by simply summing all the terms:

$$\frac{\partial^2 u(x,t)}{\partial t^2} = \frac{\partial^2 u^N(x,t)}{\partial t^2} + \frac{\partial^2 u^{IP}(x,t)}{\partial t^2} + \frac{\partial^2 u^{IS}(x,t)}{\partial t^2} + \frac{\partial^2 u^{FP}(x,t)}{\partial t^2} + \frac{\partial^2 u^{FS}(x,t)}{\partial t^2} \tag{4.8}$$

Once the total acceleration seismogram is evaluated, then, by using a numerical integration procedure velocity and displacement seismograms can be obtained.

The use of isochron formalism in the context of equation (4.8) enables us to calculate the individual contributions to the total wavefield separately, and interestingly, for the different parts of the rupture front. It is quite useful to consider this problem using the same Haskell's model, with the same parameters, as shown in Fig.4.3, and used earlier. In Fig. 4-14, the source surface for the Haskell model is shown with the projection of the receiver position on the source surface. The contributions of the four different parts of the rupture front to the total far-field displacement wavefield are shown in the insets of Fig. 4-14, along with indications of which parts of the rupture front are taking part in the calculations. Comparing displacement seismograms, even at the same distances from the receiver, one can see the shape of the waveforms undergoing quite serious changes as the rupture propagates along the source surface.

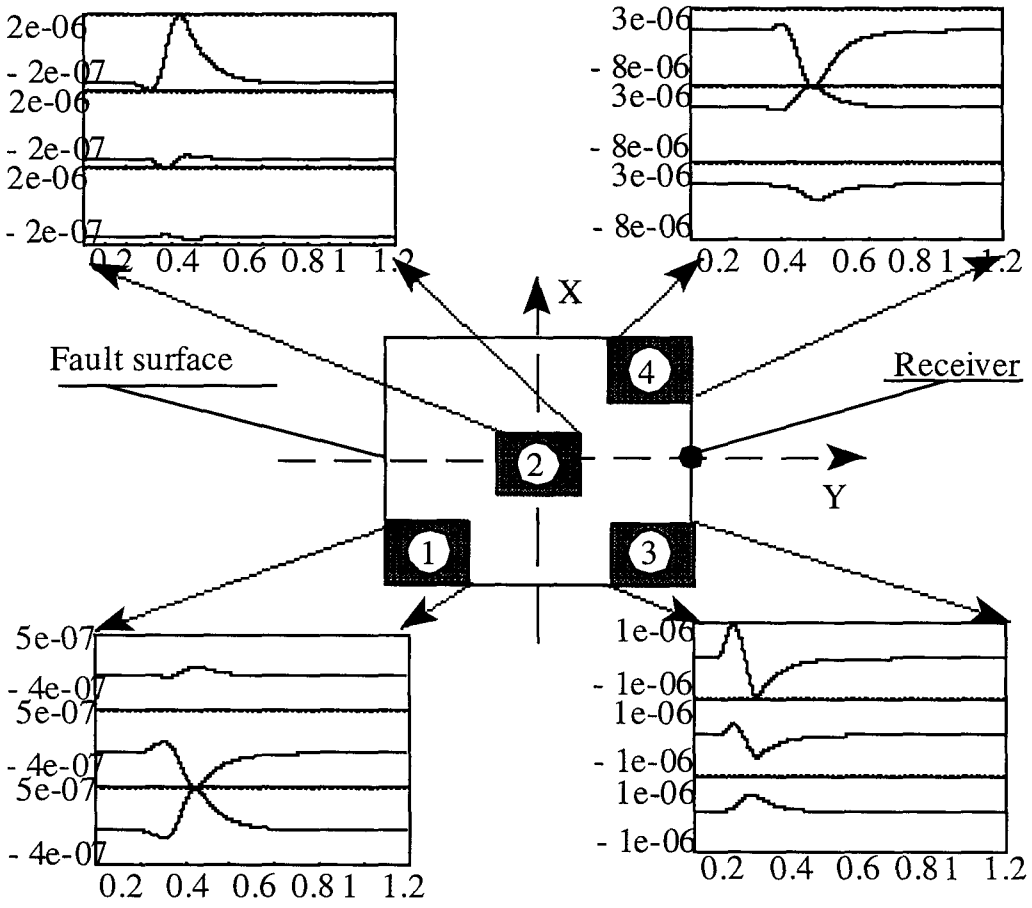

Fig.4-15. Contributions of different parts of the rupture front to the total intermediate field displacement wavefield. Projection of the receiver position onto the source surface is shown as a filled circle. The vertical units on displacement seismograms are m, while the horizontal units are s. For details of the source model and the receiver geometry see the caption to Fig. 4-3.

If one takes into account the isochron distribution for the receiver location in the Haskell's model with parameters described in the caption to Fig.4-3, then the high amplitudes of the displacement for the lower right corner subfault (marked as no.3 in Fig. 4-14) can be explained by isochron spacing, for both P and S waves (see Fig. 4-6 and 4-7 for the isochrons distribution).

Comparing the results of the synthetic calculations for the far field with the results for the intermediate field, it may be noted that much higher amplitudes are observed from the upper left corner subfault, which is marked by no.4. Still the smallest amplitudes are observed from the lower left subfault. Generally, amplitudes of synthetics for the intermediate field change quite fast, as is predicted by the representation theorem, which specifies dependence on the inverse square of the distance from the observer to the source.

Concluding this discussion of the results, it should be pointed out that the isochron integration technique combined with the powerful and fast ray-tracing synthetic seismogram computation methods can provide us with the means to attempt the source parameters inversion directly in the time domain, using all the available information from the far, intermediate and near fields and help us to gain insight into the fine structure of the rupture propagation.

5 Some applications of isochron formalism to the source parameter inversion problem.

Above isochron formalism can be applied to the source inversion problem allowing a realistic model of the source development process to obtained both in space and in time, that can explain many pecularities of the recorded wavefield.

In this section we briefly outline a possible inversion strategy for different seismic source parameters. As has been shown in the previous sections, the following parameters can be inverted:

- Rupture time distribution along the source surface;
- Final dislocation distribution;
- Rake variation along the source surface;
- Rise time distribution.

Ideally, the best solution would be to try to invert for all the specified parameters simultaneously. Unfortunately, the number of parameters for inversion makes this approach viable only for the largest events, which have been recorded by many seismic stations, in order to restrict the range of possible solutions.

All the above mentioned modelling procedures imply that the geometry of the seismic source is known. When using a single fault plane representation of the seismic source it is even possible to estimate the approximate size and shape of the event. This can be done using isochron formalism with some approximation to the source rupture mechanism, e.g. a Haskell type source

In Fig. 5-1 the maximum fracture area estimate is shown. This estimate has been obtained as the shape of the largest rupture surface compatible with the observed signal duration (separately for P and S waves) and is represented by the hatched area. The star is the position of the nucleation point. Isochrons shown in Fig. 5-3 have been calculated using the assumption of isotropic homogeneous media, and the source has been assumed to be of the circular rupture type with a constant rupture velocity equal to 0.6 V_s. Other values of rupture velociy have been also used, but 0.6 V_s gives the best fit to the observed seismograms.

The whole source area was further subdivided in 20 by 20 rectangular subfaults, and the Green's functions have been calculated using equation (4.7).

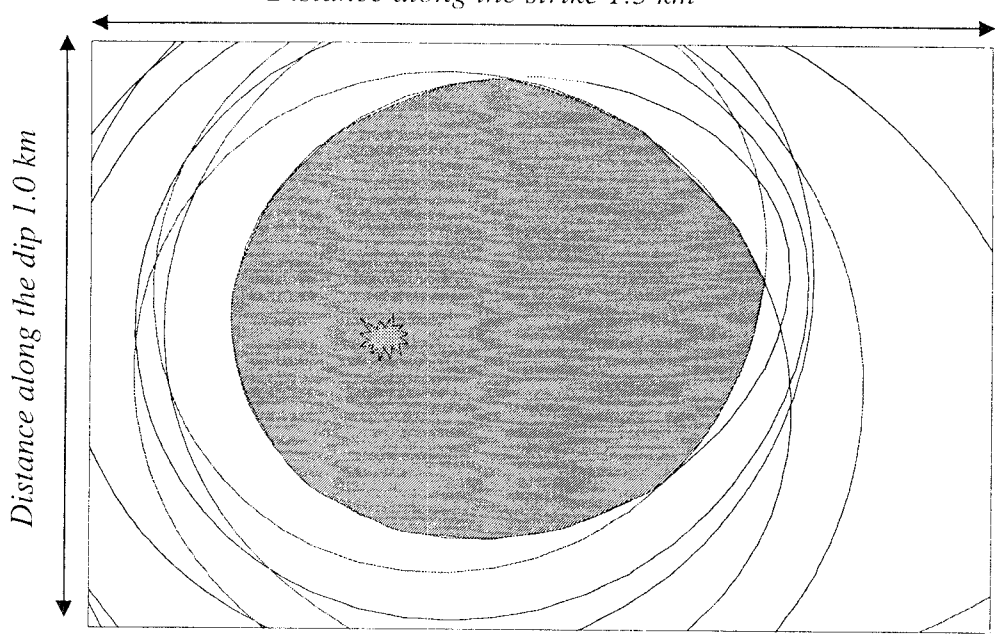

Fig.5- 1 Maximum fracture area from isochron plots. This estimate has been obtained as the shape of the largest rupture surface compatible with the observed signal duration (separately for P and S waves) and is represented by the hatched area. The star is the position of the nucleation point. Isohrons have been calculated using the assumption of isotropic homogeneous media and the source has been assumed to be of the circular rupture type with a constant rupture velocity equal to 0.6 V_s.

Different types of inversion can be undertaken:

- Inversion only for rupture times, with fixed final dislocation, rake and rise time over the whole source surface.
- Inversion for the final dislocation, which has been allowed to vary along the fault surface, while the rupture has been assumed to be a circular type, with constant rupture velocity equal to 0.6 V_s, and all other parameters assumed to be the same over the whole source surface.

- Inversion for a constant rupture velocity, assuming some source rupture propagation model, e.g. Haskell type rupture, circular rupture, etc., and constant rake, rise time and final slip value.
- Full inversion, when rupture times, final slips, rise times and rakes are allowed to vary along the source surface. This is the ideal case, but unfortunately this type of inversion can be done only for the largest events recorded by a large number of seismic stations.

In concluding this brief description of one of many possible applications of isochron formalism, it worth mentioning that calculation of a complete synthetic seismogram for one seismic station for a large fault, represented as a 20 by 20 grid of smaller size rectangular faults, takes less than a second on an SGI Impact machine.

6 Conclusions and recommendations

The tendency for denser, more sensitive seismic networks and for the deployment of accelerometers invalidates many assumptions currently used for routine seismological processing. In addition, routine source parameter inversion is usually performed in the frequency domain, discarding all the time dependent information contained in seismograms, basically restricting the inversion procedure to first arrival P and S waves and ignoring all near- and intermediate-field radiation effects. Utilising this information obviously necessitates time-domain treatment for source parameter estimation. The closeness of the seismic sources to the receivers leads to overestimation of seismic moments and unnecessary large uncertainties in the estimates of stress drop and radiated energies. The problem becomes even more complicated when taking into account the non-linearity of seismic wave propagation. The origin of this phenomenon is inelastic, large strain at the source of a propagating displacement. It is possible that up to 30 per cent of the information provided by seismic networks in our mines is lost or misinterpreted due to these problems. Thus, in order to obtain proper and more detailed estimates of seismic parameters a quite different approach to the source inversion problem must be used. One solution is time domain processing of waveforms.

With the advent of new methods for numerical modelling of wave propagation, based on ray theory, which allow selective modelling of different waves types, this type of inversion is becoming feasible. These methods, operating in time domain, afford a close match between observed and synthetic seismograms at a fraction of the computational cost usually required for this type of inversion by standard finite-difference and finite-element (FD/FE) numerical modelling procedures. Newly developed techniques allow the separate estimation of the near, intermediate and far field contributions for any receiver location and for complex sources.

The main idea is to replace the integral over the whole source surface by a sequence of line integrals along so-called isochrons. The use of isochron formalism reveals a direct link between ground acceleration, rupture acceleration and the spatial variation of slip on the fault. While the ground motion is indirectly related to rupture velocity, it is directly related to isochron velocity. Thus, the algorithm for forward modelling of seismic source radiation both in the near and the far field can be divided in two parts. For stations situated close to the source, the contributions of the far, intermediate and near fields are calculated. The initial far-field wavefront is then constructed and propagated using the

recursive cell ray tracing method. These methods, given the initial wavefront, can propagate it throughout the whole model space and can take into account multiply reflected, transmitted, converted and optionally diffracted waves to generate synthetic seismograms for the stations situated in far field. Inversion based on a ray theory is fast, as the Green's functions need only be calculated once, while for standard FD/FE techniques the functions must be recalculated for every iteration — an important consideration for routine application in mines.

The obtained results demonstrate the flexibility of the isochron formalism approach combined with ray-tracing techniques for a number of modelling and inversion applications. Advantages are obvious: apart from a significant reduction in computer time and memory requirements, these methods provide a means for obtaining a complete breakdown of the recorded wavefield, facilitating understanding and interpretation of the observed seismograms.

Furthermore, taking into account the inherent ability of ray-theory based methods to model high-frequency seismic wave propagation, the frequency range of signals to be modelled can be significantly expanded. In fact, ray-theory methods are the only ones, which can provide this kind of high-frequency information. It is computationally extremely difficult to obtain wide frequency band synthetic seismograms using FD/FE methods).

Another advantage is the use of Green's function formalism. Usually, during inversion procedures it is required that synthetics be calculated many times before convergence is achieved. From this point of view ray-theory based methods are invaluable, because the Green's functions may be computed only once for every source element used in the inversion and stored in memory, saving significant amount of computer effort.

The methodology developed now allows the formulation of processing algorithms for the time domain inversion of seismic source parameters in a fraction of the time previously required. New algorithms for source radiation modelling may be combined with the latest three dimensional raytracing algorithms for the routine calculation of synthetic seismograms and inversion of seismic source parameters.

The algorithms and techniques developed in GAP211 allow us to embark on a new project which can make routine time domain inversion feasible in the very near future. Different types of inversion can be chosen – inversion for slip velocity distribution, for rupture times, rake distribution, etc., depending on specific requirements. Time domain processing of

waveforms, recorded in the vicinity of seismic sources will provide insight into the fine structure of the source, such as slip distribution over the source surface. These parameters enable a more realistic quantification of seismicity by parameters pertaining to changes in the stress, strain rate, viscosity and diffusion of the deformation process in rock thus facilitating the integration of results of the seismic monitoring and numerical modelling.

7 References

1. Bernard, P. and R. Madariaga (1984). A new asymptotic method for the modelling of near-field accelerograms, *Bull.Seismol.Soc.Am.,* 74, pp.539-557.
2. Spudich, P. and L.N.Frazer (1984). Use of ray theory to calculate high-frequency radiation from earthquake sources having spatially variable rupture velocity and stress drop, *Bull.Seismol.Soc.Am.,* 74, pp.2061-2082.
3. Joyner W.B. and P.Spudich (1994). Including near-field terms in the isochron Integration method for the application to finite fault or Kirchoff boundary integral problems, *Bull.Seismol.Soc.Am.,* 84, pp.1260-1265.